Modeling and Design of Lattice-Reinforced Pneumatic Soft Robots

Dong Wang, Chengru Jiang, and Guoying Gu, *Senior Member, IEEE*

***Abstract*—Lattice metamaterials exhibit diverse functions and complex spatial deformations by rational structural design. Here, lattice metamaterials are exploited to design pneumatic soft robots with programmable bending, twisting, and elongation deformations. The system comprises an elastomeric tube reinforced by lattice metamaterials. We develop an analytical framework to model the twisting, bending, and elongation finite deformation taking into account the geometric orthotropy and nonlinear elasticity. We experimentally validate our modeling approach and investigate the effects of geometric patterns and input loading on the soft actuators' deformation. Theoretical guided design of lateral-climbing soft robots and exploration soft manipulators are demonstrated. The soft actuator could exhibit a combined twisting–bending–elongation deformation by lattice superimposition. The proposed structural design method paves the way for designing soft robots with complex and dexterous deformations.**

***Index Terms*—Finite deformation modeling, lateral-climbing soft robot, lattice metamaterials, pneumatic soft robots.**

I. Introduction

SOFT robotics can match or even exceed natural organisms' extraordinary versatility and multifunctionality due to their inherent compliance and design flexibility [1], [2], [3], showing promising applications in various areas, such as implantable [4] and wearable devices [5], [6], robots moving through unstructured environments [7], and grippers with conformal grasping [8]. Soft robots are driven by soft actuators, which provide diverse and dexterous motions [9], [10]. Due to the infinite degree of freedom and the nonlinear behavior of soft materials, it is still challenging to realize the controllable deformation of soft actuators [11]. Many methods have been proposed to address this issue [12], [13], [14], mainly by introducing geometric or material anisotropy [15], [16], [17], [18].

Manuscript received 24 August 2023; revised 1 November 2023; accepted 7 November 2023. Date of publication 20 November 2023; date of current version 15 December 2023. This paper was recommended for publication by Associate Editor Y. Liu and Editor A. Menciassi upon evaluation of the reviewers' comments. This work was supported in part by the National Natural Science Foundation of China under Grant 52275025, Grant 52025057, and Grant T2293725, in part by the National Key Research and Development Program of China under Grant 2022YFB4700900, and in part by the State Key Laboratory of Mechanical System and Vibration under Grant MSVZD202301). *(Dong Wang and Chengru Jiang contributed equally to this work.) (Corresponding author: Guoying Gu.)*

The authors are with the State Key Laboratory of Mechanical System and Vibration, School of Mechanical Engineering, Shanghai Jiao Tong University, Shanghai 200240, Chinaand also with the Meta Robotics Institute, Shanghai Jiao Tong University, Shanghai 200240, China (e-mail: wang_dong@sjtu.edu.cn; chengru_jiang@sjtu.edu.cn; guguoying@sjtu.edu.cn).

Digital Object Identifier 10.1109/TRO.2023.3334629

Using geometric anisotropy, pneumatic network (PneuNet) soft actuators can realize programmable deformations actuated by the inflation of a PneuNet of small channels in elastomeric materials, showing wide applications, such as multimodal grippers [19], [20], soft tentacles [21], and soft gloves [22]. Using a series of internal chambers with the same angle arranged in a row, pneumatic soft actuators that can generate bending and twisting motions simultaneously were developed [23]. Various theoretical models have been developed to model the PneuNet soft actuators. For example, de Payrebrune and O'Reilly [24] developed a theoretical model based on Euler's theory of the elastic to capture the non-constant curvature deformation of the PneuNet soft actuators. Jiang et al. [25] developed a finite deformation model to inverse design the 3-D trajectories of multisegment PneuNet soft manipulators. Geometric anisotropy generally involves small cavities with complex structures, complicating the fabrications.

Material anisotropy uses the modulus differences in different materials to form controllable motions. A typical example using material anisotropy is the McKibben actuators, consisting of an elastomeric tube wrapped in inextensible fibers [26], [27]. The McKibben actuators show 1-D elongation or contraction depending on the tilted angles of the wrapped fibers [28]. By changing the wrapping pattern of the fibers, fiber-reinforced soft actuators have been developed to exhibit spatial bending, twisting, elongation, and expansion motions [29], [30], [31]. Inspired by the muscle fiber arrangement, pneumatic soft actuators showing bending and helical deformations were realized by combining braided tubes and reinforced flexible frames in different orientations [32]. In addition to reinforced fibers, constraint layers and elastomers have been utilized to introduce anisotropy and control the deformation of soft actuators. For instance, Shah et al. [33] have developed reconfigurable stiffness-changing skins capable of stretching and folding, creating various 3-D structures. Moreover, paper has been employed to introduce anisotropy into elastomers, effectively increasing the stiffness and functionalities of soft actuators [34]. Another proposed design is the slit-in-tube actuators, which consist of an elastomeric balloon enclosed by an external shell containing slits of varying directions and lengths, enabling bending, twisting, contraction, and elongation motions [35], [36]. Several theoretical models have been developed. For instance, Connolly et al. [31] presented a strategy based on nonlinear analytical modeling and optimization to design fiber-reinforced soft actuators following particular trajectories. However, the nonstretchability and noncompressibility of fibers limit the formation of complex patterns and motions.

Lattice metamaterials can form diverse programmable deformations by tuning the geometric patterns, providing a promising way to program soft actuators [37], [38], [39]. In contrast to the reinforced fibers, the lattice layer can provide diverse patterns and is easier to fabricate. Compared with the previous reported constraint layers and elastomers, the lattice layer offers higher design flexibility, allowing for the formation of complex patterns that were previously challenging to achieve. Patterns include periodic curled microstructures, multiple sets of aligned grids, and structures with varying geometric parameters. Furthermore, the lattice layer is self-supportable and structural stable. Serial connection or lattice superimposition is also feasible due to the high freedom of structural design, enabling dexterous motions. However, it is still unclear how to integrate lattice metamaterials in soft actuators to realize controllable deformation and motions. The development of theoretical models is also difficult due to the complex lattice patterns and finite deformation.

In this work, we proposed a lattice-reinforced method to control the deformation of pneumatic soft actuators. The lattice-reinforced soft actuators can realize bending, twisting, and elongation deformation using various reinforced lattices. We develop a nonlinear theoretical framework to predict finite deformations, considering geometric orthotropy and nonlinear elasticity. The effects of geometric patterns, microstructures' orientation angles, and differential thickness are studied using the theoretical model. Experiments show that the proposed lattice-reinforced method can control the motions with high repeatability and validate the theoretical model. Results show that various trajectories can be programmed by varying the geometric patterns and applied loadings. In particular, the twisting is maximized when the tilted angle is around 36°, while the soft actuators exhibit pure elongation when the tilted angle of two grids is supplementary. The high geometric freedom of the lattice metamaterials also enables the serial connection or superimposition of various geometric patterns. Theoretical guided design of two-segment lateral-climbing soft robots and exploration soft manipulators are demonstrated. By utilizing the lattice superimposition, we develop a soft actuator with a combined twisting–bending–elongation deformation.

The main contributions of this work can be summarized as follows.

1) We propose a method to realize the bending, twisting, and elongation deformations of pneumatic soft actuators by designing the patterns of lattice-reinforced layers.
2) We develop an analytical framework to model the twisting, bending, and elongation deformations considering the geometric orthotropy and nonlinear elasticity, and validated using experiments.
3) We investigate the effects of geometric patterns and input loading on the soft actuators' deformation and demonstrate lateral-climbing soft robots and exploration soft manipulators based on the numerical results.

The rest of this article is organized as follows. Section II introduces the geometric design. The theoretical model is presented in Section III and validated in Section IV. Section V provides the dynamic responses. Numerical results are given in Section VI. Designed soft robots are demonstrated in Section VII. Finally, Section VIII concludes this article.

II. Geometric Design

Twisting, elongation, and bending soft actuators are designed as shown in Fig. 1. The lattice-reinforced soft actuator consists of a silicone tube as the inner layer and a reinforced lattice as the constraint layer. Air pressure is applied from one end of the silicone tube. Upon inflation, the soft actuators exhibit various deformations depending on the geometric design of the lattice layer. The lattice of the twisting soft actuator consists of a set of tilted grids with an orientation angle α and a set of circular grids. The tilted grid is to guide the actuators' twisting motion, while the circular grid is used to restrict the radial expansion. Under an input pressure P, the soft actuator shows both twist and elongate deformations. The amount of twisting is determined by the orientation α. The elongation soft actuator is designed by distributing a set of horseshoe-shaped units vertically [see Fig. 1(b)]. The lattice is highly stretchable as the horseshoe microstructures bend and uncurl upon inflation, leading to an elongation deformation. The soft actuator exhibits a bending deformation when different widths w are used on each side [see Fig. 1(c)]. The thinner part extends more and the thicker part extends less when inflated. The differential elongation drives the soft actuator to bend toward the thicker part.

The general guideline for choosing the lattice shapes is shown below. For twisting soft actuators, tension-twisting coupled structures are required. In our work, we have utilized the tilted grid. The tilted grid demonstrates a tension-twisting coupled effect, enabling the actuator to twist under tension. Curved structures, such as spirals, horseshoes, and wavy designs, are commonly used for elongation soft actuators. The curved structures bend, rotate, uncurl, and align to the loading directions and resist excessive loadings by stretching. Therefore, the stretchabilities are significantly increased. We have chosen the horseshoe structure among these options due to its simplicity and constant curvature. In the case of bending soft actuators, differential stiffness is crucial. Structures with varying widths can be employed, allowing for differential bending behavior. This straightforward lattice design provides a practical solution for achieving diverse motions.

III. Theoretical Modeling

To accurately control the soft actuators' deformation, theoretical models are developed for the bending, elongation and twisting deformation. We develop a finite deformation model based on orthotropic constitutive equations to study the twisting soft actuators. The isotropic neo-Hookean energy density function is used for inner layer. An anisotropic energy density function that considers the elongation and bending energy of the reinforced grids is used for the lattice layer. The governing equations are derived from the Cauchy equilibrium equations, which are combined with the force and moment balance equations to solve the deformation of the twisting actuators. A bending model based on the force and moment balance at the top surface is developed. The nonlinear stress-strain curves of the horseshoe

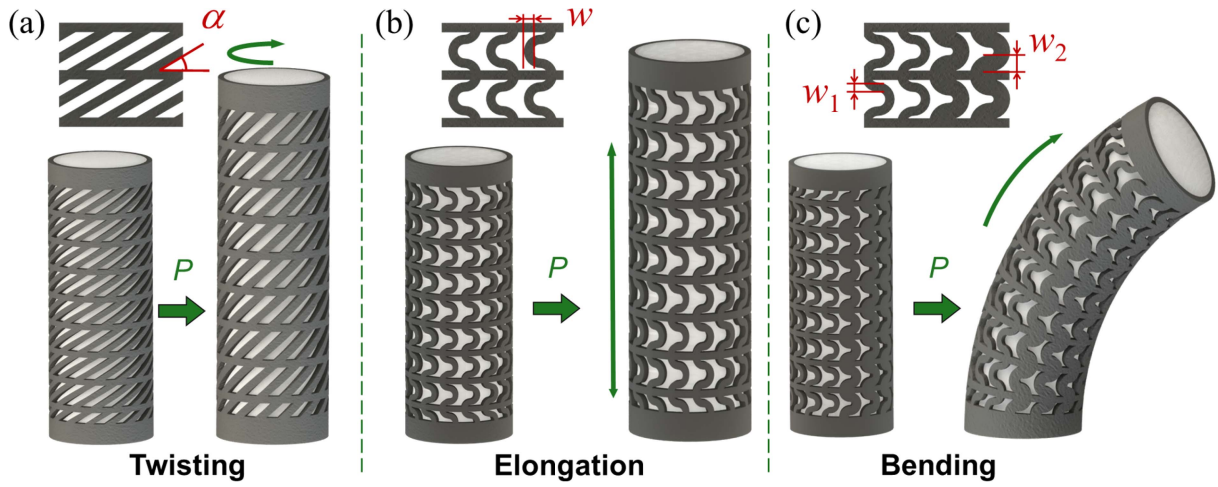

Fig. 1. Geometric design of lattice-reinforced soft actuators. Soft actuator consists of a silicone tube inner layer and a reinforced lattice layer. (a) Lattice layer of the twisting soft actuator consists of a set of tilted grids with an orientation angle α and a set of circular grids. (b) Elongation deformation is generated by distributing a set of horseshoe-shaped units vertically. (c) Soft actuator exhibits bending deformation when the widths w are different on each side.

structure of the lattice layer is taken into account. The elongation actuators are modeled as a particular case of the bending model with uniform widths.

A. Model of Twisting Soft Actuators

The twisting soft actuator consists of an isotropic silicone inner layer and an anisotropic lattice layer. The energy density function can be written as the sum of the two parts

$$W_t = c_1 W_t^{(\text{iso})} + c_2 W_t^{(\text{aniso})} \tag{1}$$

where c_1 and $c_2 = 1 - c_1$ are the volume fractions of the inner silicone and outer lattice, respectively. $W_t^{(\text{iso})}$ and $W_t^{(\text{aniso})}$ are the energy density functions of the isotropic inner silicone and anisotropic outer lattice. For the isotropic inner silicone, we choose an incompressible neo-Hookean model [40]

$$W_t^{(\text{iso})} = \frac{\mu}{2}(I_1 - 3) \tag{2}$$

where $I_1 = tr(\boldsymbol{F}\boldsymbol{F}^T)$ and μ denotes the shear modulus of the silicone material. $\boldsymbol{F}$ is the deformation gradient. The anisotropic lattice layer is formed by a set of tilted grids with an orientation angle α and a set of circular grids. The stretching energy density function of the anisotropic lattice layer is [31]

$$W_t^{(\text{aniso})(s)} = \frac{(\sqrt{I_4} - 1)^2 E}{2} + \frac{(\sqrt{I_6} - 1)^2 E}{2}. \tag{3}$$

The two terms on the right-hand side represent the energy density functions of the tilted grids and circular grids, respectively. $I_4 = \boldsymbol{F}\boldsymbol{A}_1 \cdot \boldsymbol{F}\boldsymbol{A}_1$ and $I_6 = \boldsymbol{F}\boldsymbol{A}_2 \cdot \boldsymbol{F}\boldsymbol{A}_2$ are pseudoinvariants to characterize the orthotropies generated by the grids. $\boldsymbol{A}_1 = (0, \cos\alpha, \sin\alpha)$ and $\boldsymbol{A}_2 = (0, 1, 0)$ are the direction vectors of the tilted and circular grids in the undeformed configuration. E is the lattice material's Young's modulus. We observe experimentally that the tilted grids will not only rotate and elongate, but also bends due to the overlap with circular constraints during actuation. Fig. 19 shows that the bends mainly exist at the joints of the tilted and circular grids. Therefore, the tangential bending energy should also be considered. The bending energy of a grid unit is expressed in the form of a linear spring. Therefore, the bending energy density function can be written as [41]

$$W_t^{(\text{aniso})(b)} = \frac{k_t {\theta_t}^2}{2\,V}. \tag{4}$$

The spring stiffness k_t is equivalent to the flexural rigidity of an antisymmetric bending beam by correlating to the beam theory with linear elasticity such that $k_t = \frac{12EI}{L_t}$ [41]. EI/L_t is the flexural rigidity of the grid unit, where I and L_t denote the cross-sectional moment of inertia and length. $\theta_t = \arccos(\frac{A_1 \cdot F A_1}{\sqrt{A_1 \cdot F^T \cdot F \cdot A_1}})$ is the rotation angle after tilting, which is shown in Fig. 19(d). V is the volume of the grid unit.

The strain energy density function of the twisting soft actuator is then

$$\begin{aligned} W_t &= W_t^{(\text{aniso})(s)} + W_t^{(\text{aniso})(b)} \\ &= c_1 \frac{\mu}{2}(\mathbf{I}_1 - 3) \\ &\quad + c_2 \left(\frac{(\sqrt{\mathbf{I}_4} - 1)^2 E_t}{2} + \frac{(\sqrt{\mathbf{I}_6} - 1)^2 E_t}{2} + \frac{k_t {\theta_t}^2}{2\,V} \right). \end{aligned} \tag{5}$$

Besides the twisting, the lattice-reinforced twisting actuator also exhibits an extension in the length direction and expansion in the radial direction when inflated. A pressure P is applied on the inner silicone tube, while the outer surface is assumed to be traction-free. Cylindrical coordinates are used. The reference and current cylindrical coordinates are denoted as (R, Θ, Z) and (r, θ, z), respectively. Uniform stretches in the length direction and radial direction are assumed based on experimental observations, defined as λ_t and λ_θ, respectively. The twist per unit length is defined as τ. Thus, the current and reference coordinates can be related by the deformation as

$$r = \lambda_\theta R, \theta = \Theta + \tau \lambda_t Z, z = \lambda_t Z. \tag{6}$$

The incompressible constraint requires that

$$\pi({r_o}^2-{r_i}^2)l=\pi{\lambda_\theta}^2({R_o}^2-{R_i}^2)\lambda_t L=\pi({R_o}^2-{R_i}^2)L \tag{7}$$

where R_i and R_o are the inner and outer radii before deformation while r_i and r_o are the radii after deformation. L and l are the length before and after deformation. The relation between λ_θ and λ_t can be obtained as ${\lambda_\theta}^2=1/\lambda_t$. The deformation gradient $\boldsymbol{F}$ now takes the form

$$\boldsymbol{F}=\begin{pmatrix}\frac{\partial r}{\partial R} & \frac{1}{R}\frac{\partial r}{\partial \Theta} & \frac{\partial r}{\partial Z}\\ r\frac{\partial \theta}{\partial R} & \frac{r}{R}\frac{\partial \theta}{\partial \Theta} & r\frac{\partial \theta}{\partial Z}\\ \frac{\partial z}{\partial R} & \frac{1}{R}\frac{\partial z}{\partial \Theta} & \frac{\partial z}{\partial Z}\end{pmatrix}=\begin{pmatrix}\frac{R}{r\lambda_t} & 0 & 0\\ 0 & \frac{r}{R} & r\tau\lambda_t\\ 0 & 0 & \lambda_t\end{pmatrix}. \tag{8}$$

The Cauchy stresses thus can be obtained as [42]

$$\boldsymbol{\sigma}=2\frac{\partial W_t}{\partial I_1}\boldsymbol{B}+2\frac{\partial W_t}{\partial I_4}\boldsymbol{s}_1\otimes\boldsymbol{s}_1+2\frac{\partial W_t}{\partial I_6}\boldsymbol{s}_2\otimes\boldsymbol{s}_2-p\boldsymbol{I} \tag{9}$$

where $\boldsymbol{I}$ is the identity matrix; p is a Lagrange multiplier to ensure incompressibility; $\boldsymbol{B}=\boldsymbol{F}\boldsymbol{F}^T$, $\boldsymbol{s}_1=\boldsymbol{F}\boldsymbol{A}_1$, and $\boldsymbol{s}_2=\boldsymbol{F}\boldsymbol{A}_2$. $\otimes$ presents the tensor product. The Cauchy stress can then be written explicitly in the matrix form

$$\sigma=\begin{pmatrix}\sigma_{rr} & 0 & 0\\ 0 & \sigma_{\theta\theta} & \sigma_{\theta z}\\ 0 & \sigma_{z\theta} & \sigma_{zz}\end{pmatrix}. \tag{10}$$

The explicit form of the stress terms are given in Appendix B. Substituting the above stresses into the following three Cauchy equilibrium equations in r, θ and z directions

$$\frac{\partial\sigma_{rr}}{\partial r}+\frac{1}{r}\frac{\partial\sigma_{r\theta}}{\partial\theta}+\frac{\partial\sigma_{rz}}{\partial z}+\frac{1}{r}(\sigma_{rr}-\sigma_{\theta\theta})=0 \tag{11}$$

$$\frac{\partial\sigma_{r\theta}}{\partial r}+\frac{1}{r}\frac{\partial\sigma_{\theta\theta}}{\partial\theta}+\frac{\partial\sigma_{\theta z}}{\partial z}+\frac{2}{r}\sigma_{r\theta}=0 \tag{12}$$

$$\frac{\partial\sigma_{rz}}{\partial r}+\frac{1}{r}\frac{\partial\sigma_{\theta z}}{\partial\theta}+\frac{\partial\sigma_{zz}}{\partial z}+\frac{1}{r}\sigma_{rz}=0 \tag{13}$$

we can obtain one nonvanishing equation

$$\frac{d\sigma_{rr}}{dr}=\frac{\sigma_{\theta\theta}-\sigma_{rr}}{r}. \tag{14}$$

The following three boundary conditions on the applied loadings are used.

BC1: The pressure difference between the outer and inner surface is P, i.e.,

$$P=\sigma_{rr}(r=r_o)-\sigma_{rr}(r=r_i). \tag{15}$$

Substituting (14) into (15) yields

$$P=\int_{r_i}^{r_o}\frac{\sigma_{\theta\theta}-\sigma_{rr}}{r}dr. \tag{16}$$

BC2: The axial load N at the ends of the soft actuators is

$$N=2\pi\int_{r_i}^{r_o}\sigma_{zz}(r=r_o)\times rdr=P\pi{r_i}^2. \tag{17}$$

BC3: No external moment M is applied on the ends of the soft actuators

$$M=2\pi\int_{r_i}^{r_o}\sigma_{\theta z}(r=r_o)\times r^2dr=0. \tag{18}$$

Using the identities [42]

$$\sigma_{\theta\theta}-\sigma_{rr}=\lambda_\theta\frac{\partial W_t}{\partial\lambda_\theta}+\gamma\frac{\partial W_t}{\partial\gamma}$$

$$\sigma_{\theta\theta}+\sigma_{zz}-2\sigma_{rr}=\lambda_\theta\frac{\partial W_t}{\partial\lambda_\theta}+\lambda_t\frac{\partial W_t}{\partial\lambda_t}$$

$$\sigma_{\theta z}=\frac{\partial W_t}{\partial\gamma} \tag{19}$$

we can write (16)–(18) in terms of the strain energy as

(BC1)

$$P=\int_{r_i}^{r_o}\left(\lambda_\theta\frac{\partial W_t}{\partial\lambda_\theta}+\gamma\frac{\partial W_t}{\partial\gamma}\right)\frac{dr}{r}. \tag{20}$$

(BC2)

$$N=\pi\int_{r_i}^{r_o}\left(2\lambda_t\frac{\partial W_t}{\partial\lambda_t}-\lambda_\theta\frac{\partial W_t}{\partial\lambda_\theta}-3\gamma\frac{\partial W_t}{\partial\gamma}\right)rdr+P\pi r_i^2. \tag{21}$$

(BC3)

$$M=2\pi\int_{r_i}^{r_o}\frac{\partial W_t}{\partial\gamma}r^2dr. \tag{22}$$

By substituting (5) into the three boundary conditions (20)–(22), the three parameters τ, λ_t, and P can be solved numerically. The deformed shapes can then be obtained. In detail, the deformed length of the tube is obtained as $l=\lambda_t L$; the twisting per unit length is τ; the expansion in the radial direction $r=\lambda_\theta R=\sqrt{1/\lambda_t}R$.

B. Models of Bending and Elongation Soft Actuators

The bending deformation results from the differential elongations of horseshoe microstructures with different widths on both sides [see Fig. 2(d)]. The bending actuator comprises the internal silicone cylinder and the outer rubber skeleton. A pressure P is applied to the inner surface, and the external skeleton constrains the deformation of the inner silicone. We assume that the bending is uniform. R_b and θ are the radius and angle of the central axis after inflation [see Fig. 2(f)]. x is the axial direction along the centerline. y denotes the radial direction, whose origin is located at the centerline. The axial strain can then be written as

$$\varepsilon_s=\frac{(R_b+y)\theta-L_0}{L_0}=\frac{(R_b+r_b\sin\alpha)\theta}{L_0}-1 \tag{23}$$

where r_b and α denoting the radius and angular in the polar coordinates of the cross-section as shown in Fig. 2(e). L_0 is the initial length of the actuator. The axial force F_s acting on the silicone can be obtained by integrating the stress σ_s over the cross-section A_b as

$$F_s=\int\sigma_s dA_b=\int_0^{2\pi}\int_{r_i}^{r_o}E_s\varepsilon_s r_b dr_b d\alpha. \tag{24}$$

The reinforced lattice contains multiple horseshoe structures with different widths. The number of the horseshoe structures

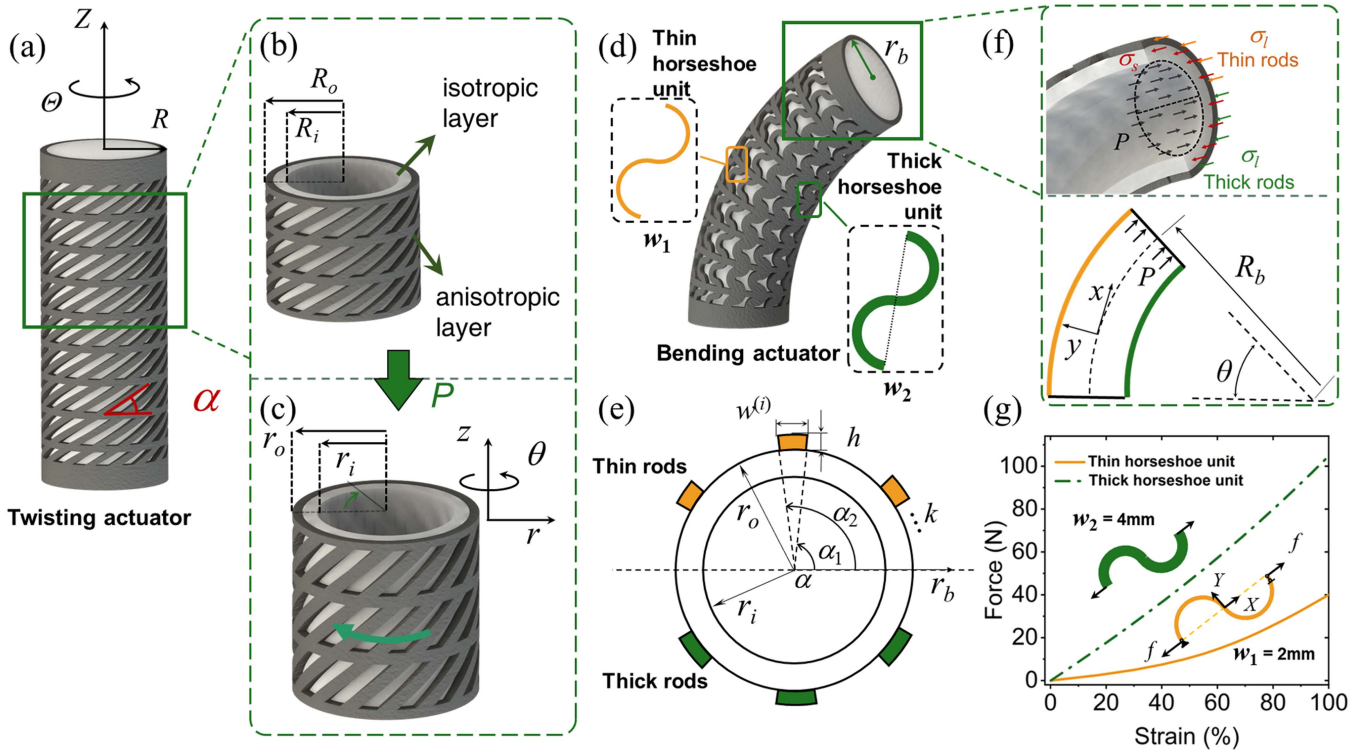

Fig. 2. Theoretical models. (a) Twisting soft actuator with orientation angle α in the undeformed state. (b) Undeformed and (c) deformed shapes under inflation. Bending theoretical model. (d) Deformed shapes of a bending soft actuator. Elongations of the horseshoe microstructures on both sides differ due to the width differences. (e) Cross-sectional view of the bending actuator. k effective rods are used to represent the thicker and thinner parts for simplification. (f) Schematic of the bending actuator. (g) Force-strain curves of two horseshoe microstructures with $w_1 = 2$ mm and $w_2 = 4$ mm. Every horseshoe microstructure is under a horizontal force f at each end.

is k. The height and width are h and $w^{(i)}$ for the ith horseshoe structure [see Fig. 2(e)]. Consider a horseshoe microstructure simply supported and deformed under horizontal force f at each end [see Fig. 2(g)]. Using the force and moment balances, the force-strain relationship of the horseshoe structure can be numerically obtained [37]. Here, we write the force-strain relationship as a function of the axial strain ε and width w as

$$f = f(\varepsilon, w). \tag{25}$$

Fig. 2(g) plots the force-strain relationship of two horseshoe microstructures with $w_1 = 2$ mm and $w_2 = 4$ mm widths under uniaxial tensile forces. The horseshoe microstructures exhibit nonlinear stress-strain curves. The effective stress of the ith horseshoe structure can then be written as $\sigma_l^{(i)} = f(\varepsilon_l^{(i)}, w^{(i)})/(hw^{(i)})$, where the axial strain of the ith horseshoe structure is obtained by substituting $\alpha^{(i)} = \frac{\alpha_1^{(i)} + \alpha_2^{(i)}}{2}$ [see Fig. 2(e)] into (23) as $\varepsilon_l^{(i)} = \frac{(R_b + r_o \sin\alpha^{(i)})\theta}{L_0} - 1$. The axial force $F^{(i)}$ generated by the ith horseshoe structure can then be integrated as follows:

$$F^{(i)} = \int \sigma_l^{(i)} dA_b = \int_{\alpha_1^{(i)}}^{\alpha_2^{(i)}} \int_{r_o}^{r_o+h} \sigma_l^{(i)} r_b dr_b d\alpha. \tag{26}$$

The force and moment balances on the upper surface of the bending soft actuator require

$$\begin{cases} P\pi r_i^2 = F_s + F_l, \\ M = \int \sigma_s \times r_b \sin(\alpha) dA_b \\ \quad + \sum_{i=1}^{k} \int \sigma_l^{(i)} \times r_b \sin(\alpha^{(i)}) dA_b = 0. \end{cases} \tag{27}$$

By substituting (23)–(26) into the equilibrium (27), the two parameters R_b and θ can be solved numerically in MATLAB.

C. Shape Reconstruction

The centerline of a lattice-reinforced soft actuator can be described by each segment joint together, with the length and radial directions changing continuously at the interface. Therefore, each segment except the first one needs to be transformed by a rotation matrix. We denote the initial coordinates as $\boldsymbol{T}^{(j)}$ and the transformation matrix between the beginning and end orientations of jth segment as $\boldsymbol{R}^{(j)}$. The final coordinates of the mth segment are then

$$\text{if } j = 1, \boldsymbol{T}_{\text{final}}^{(j)} = \boldsymbol{T}^{(1)} \tag{28}$$

$$\text{for } j \geq 2, \boldsymbol{T}_{\text{final}}^{(m)} = \prod_{j=1}^{m-1} \boldsymbol{R}^{(j)} \boldsymbol{T}^{(m)} + \boldsymbol{T}_{\text{final}}^{(m-1)}. \tag{29}$$

Using the above rule, the centerline of the 3-D shapes is reconstructed. The final deformed shape can be built by mapping the points on the centerline along the radial direction. We use

MATLAB to plot the 3-D shape of the lattice-reinforced soft actuator.

IV. Experimental Validation

We validate the theoretical predictions with experiments in this section. The elongation, bending, and twisting theoretical models are implemented in MATHEMATICA and MATLAB code. The code is run on a desktop with an AMD Ryzen 5 3600 CPU @3.60 GHz processor with 16 GB RAM. The total computer time for a single calculation is generally less than 30 s.

The fabrication procedures of the lattice-reinforced actuators are given in the Appendix E. Both the outer lattice structures and inner silicone are fabricated by molding. A commercially available polyurethane-based rubber, Hei-Cast 8400 (Shore 90 A), is used for the outer lattice. Ecoflex 00-50 is used for the inner tube. The Young's moduli of Hei-Cast are measured as 19.46 MPa [43]. The shear modulus of the silicone material (Ecoflex 00-50) of measured as around $\mu = 0.08$ MPa. The two ends of both structures are glued together. The pressure is applied from one end using an air pump. The volume fractions of the inner silicone and outer lattice are calculated as around $c_1 = 0.91$ and $c_2 = 0.09$, respectively.

A. Experimental Setup

We have built an experimental stage to measure the actuation performances of the soft actuators [see Fig. 3(a)]. The input pressure is generated from a pneumatic cabinet, controlled by the digital signals from dSPACE. An industrial camera (MERCURY2, Da Heng Imaging) is used to capture the deformations of the actuators. The deformation data is extracted with the motion capture software Kinovea.

For the bending actuators, we have built an experimental platform [see Fig. 3(b)] to analyze the block forces of the proposed actuators. For the twisting actuator, we proposed an axially rotatable force-measuring platform to test the output torque of the actuator [see Fig. 3(c)]. The analog signal from the torque sensor is amplified and displayed on the oscilloscope.

B. Elongating and Bending Model Validation

The elongation and bending models are validated first. Elongation and bending soft actuators are fabricated with width ratios $n = 2{:}2, 2{:}2.5, 2{:}3$, and $2{:}3.5$. The width of the thinner horseshoe microstructure is set as 2 mm. The width and interval of the circular grids are set as 2 and 10 mm, respectively. The thickness of the lattice structure is 2 mm.

Fig. 4(a)–(d) shows the shapes of the four soft actuators before and after inflation ($P = 30$ kPa) (is presented in Supplementary Video S1). The soft actuators exhibit pure elongating deformation when the width ratio is 2:2, while the soft actuators with nonuniform widths show bending and elongating simultaneously. The corresponding theoretical shapes are plotted in Fig. 4(e)–(h) for comparison. It can be observed that the theoretical predictions agree well with the experimental deformed shapes. For quantitative comparison, Fig. 4(i) compares the theoretical and experimental bending angle θ as a function of the applied pressure. The experimental and theoretical θ agree well when the width ratio changes from 2:2 to 2:3.5. θ increases with the width of the thicker horseshoe and nonlinearly with the pressure P. Note that no fitting parameter is used in the bending model.

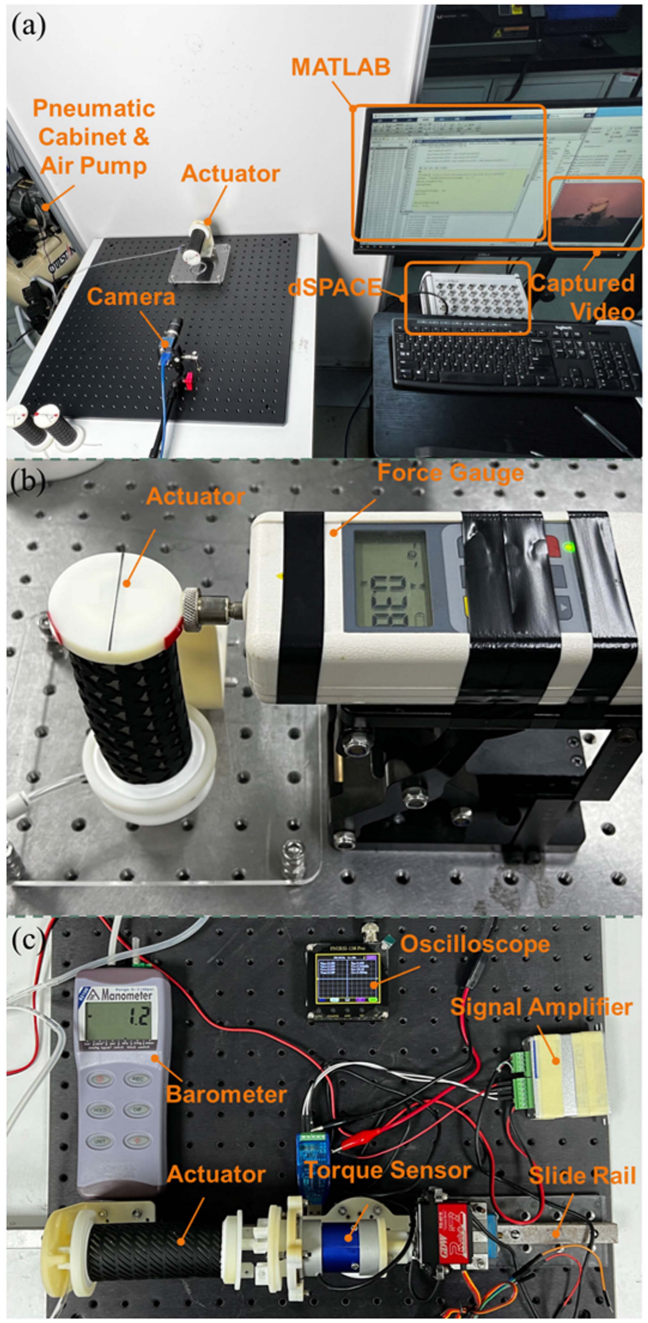

Fig. 3. Experimental stages for the actuation performances. (a) Digital signals from dSPACE control the applied pressure from the pneumatic cabinet. (b) Experimental bending force-measuring platform. Output forces of the actuators are displayed on the electronic manometer. (c) Experimental axially rotatable force-measuring platform. Analog signal from the torque sensor is amplified and displayed on the oscilloscope.

C. Twisting Model Validation

Twisting soft actuators with orientation angles $\alpha = 30°, 45°$, and $60°$ are fabricated and tested (Video S1). The thickness of the grids is 2 mm. The numbers of the tilted grids and circular grids

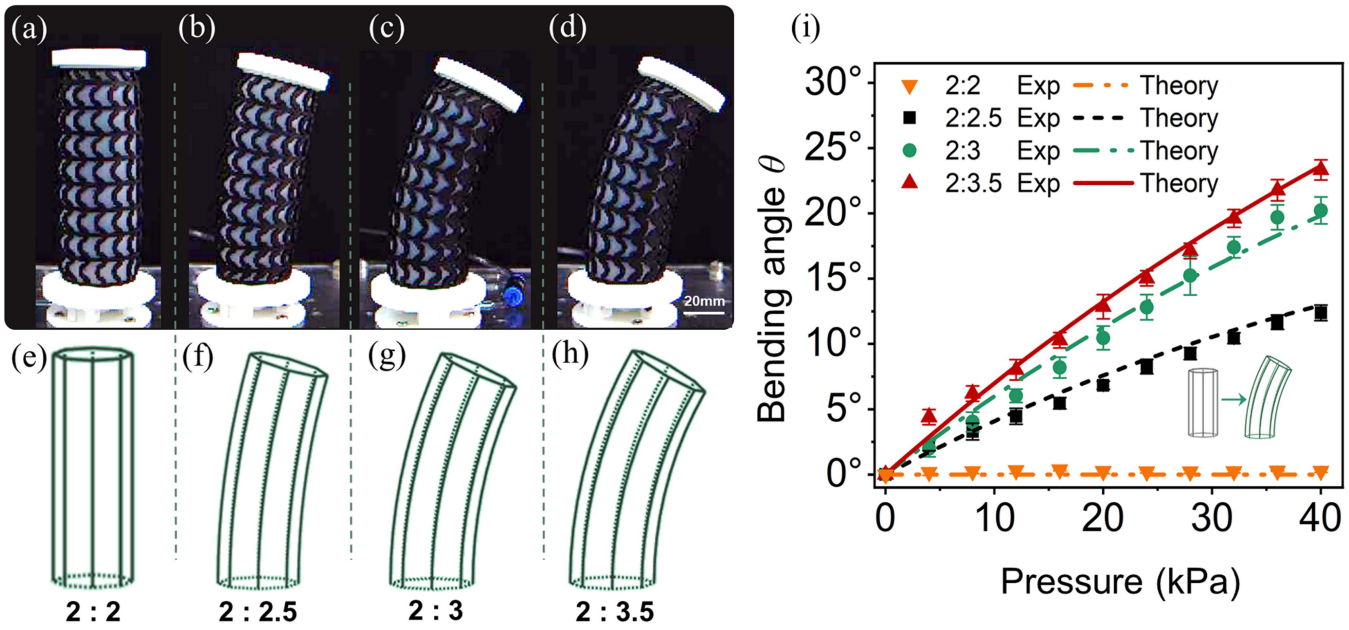

Fig. 4. Validation of elongation and bending model. (a)–(d) Shapes of elongation and bending soft actuators under $P = 30$ kPa. Width ratios are $n = 2{:}2$, 2:2.5, 2:3, 2:3.5, respectively. (e)–(h) Corresponding theoretical deformed shapes. (i) Comparison between theoretical (curves) and experimental (markers) bending angle θ as a function of P. Ten tests were conducted for each soft actuator. Error bars represent the standard deviation.

are both 8. The deformed shapes under $P = 40$ kPa are shown in Fig. 5(a)–(c). All three soft actuators exhibit a combined twisting and elongation. The theoretical predicted deformed shapes are shown below in Fig. 5(d)–(f).

Two parameters are used to characterize the deformation: the twist per unit length τ (rad/mm) and the axial strain λ_t. τ is measured by the mark lines on the top end of the soft actuator [see Fig. 5(c)], and axial strain λ_t is measured from the front view pictures using ImageJ. The experimental and theoretical τ are compared for soft actuators with $\alpha = 30°$, $45°$, and $60°$ in Fig. 5(g)–(i). The experimental τ agrees well with the theoretical prediction, which means that the nonlinear constitutive equation can adequately characterize the finite twisting deformation of the lattice-reinforced soft actuators. Some discrepancies exist between experimental and theoretical τ when $\alpha = 30°$, possibly due to the overlaps between the tilted and circular grids.

Fig. 5(j) compares the experimental and theoretical λ_t. λ_t increases with the pressure P almost linearly. The theoretically predicted λ_t agrees well with the experiments when $\alpha = 45°$ and $30°$. Some discrepancies exist when $\alpha = 60°$, possibly due to the radial expansion and the bulging. The theoretical predicted λ_t and τ are 3-D plotted as functions of P and α in Fig. 5(k) and (l). λ_t reaches its maximum value when $\alpha = 0°$, which means the tilted grids become circular. The twisting soft actuators have been optimized based on the theoretical model. Fig. 5(k) shows that the theoretical predicted τ reaches its maximum value when $\alpha = \sim 36°$, which means highest torsional efficiency. We have fabricated twisting soft actuators with $\alpha = 36°$ and measured the twisting angle under various P (see Fig. 6). We can observe that the twisting angle is larger than $\alpha = 30°$, $45°$, and $60°$, and the magnitudes match well with the numerical prediction. The maximum twisting angle τ at $\alpha = \sim 36°$ agrees well with the magic angle predicted by previous work [44], [45].

V. Dynamic Response

The actuation performances are measured and evaluated here including the controllability, repeatability, bandwidth, speed performances, and output forces of the soft actuators.

Sweeping frequency tests are conducted to investigate the dynamic response of the proposed soft actuators. An exciting pressure P_{sweep} is applied with

$$P_{\text{sweep}} = \frac{A}{2}\sin\left(2\pi\frac{(1-0.01)t+0.01}{120}t - \frac{\pi}{2}\right) + \frac{A}{2} \quad (30)$$

where the amplitude $A = 40$ kPa. The frequency increases from 0.01 to 1 Hz in 120 s. Fig. 7(a) shows the change of the normalized bending angles with time for three bending actuators with the width ratio from 2:2.5 to 2:3.5. Fig. 7(b) demonstrates the effect of applied frequency on the twisting angle of three twisting actuators with $\alpha = 30°$, $45°$, and $60°$. As the frequency of the applied pressure increases, the higher amplitudes of the bending and twisting angles decrease and the lower amplitudes increase. From the dynamic response, we can estimate the bandwidths are 0–0.23 Hz, 0–0.25 Hz, 0–0.24 Hz for bending soft actuators with $n = 2{:}2.5$, 2:3, and 2:3.5, respectively. The bandwidths are 0–0.17 Hz, 0-0.25 Hz, and 0-0.31 Hz for twisting soft actuators with $\alpha = 30°$, $45°$, and $60°$, respectively.

The loading and unloading behaviors of the bending and twisting soft actuators are tested to explore their repeatability. A sinusoidal pressure with different frequencies is applied to the

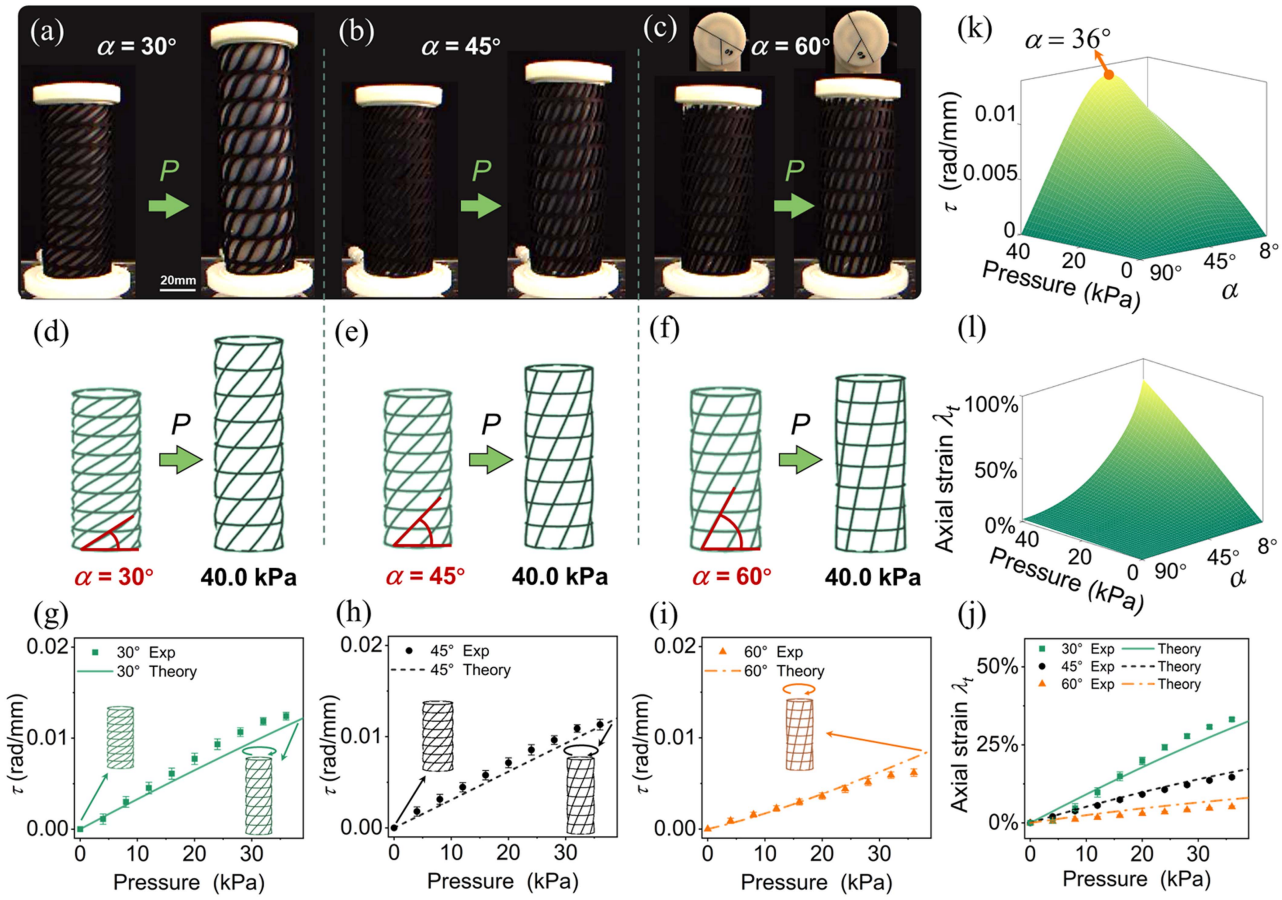

Fig. 5. Validation of the twisting model. (a)–(c) Deformed shapes of twisting soft actuators with $\alpha = 30°, 45°$, and $60°$ under $P = 40$ kPa. (d)–(f) Corresponding theoretical predicted shapes. (g)–(j) Comparison between theoretical (curves) and experimental (markers) twist per unit length τ and axial strain λ_t as a function of P. (k, l) Theoretical predicted 3-D plot of τ and λ_t on P and α. Ten tests were conducted for each soft actuator. Error bars represent the standard deviation.

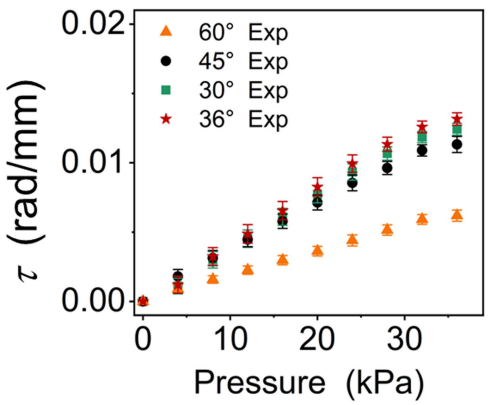

Fig. 6. Experimental results of the twisting actuators when the tilted angle $\alpha = 60°, 45°, 30°$ and $36°$.

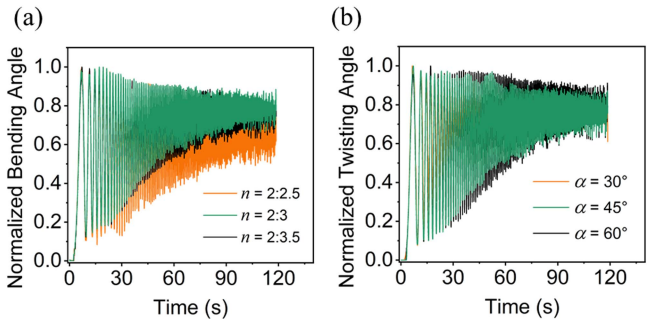

Fig. 7. Frequency response of bending and twisting actuators. An exciting pressure is applied, and the frequency increases from 0.01 to 1 Hz in 120 s. (a) Dependence of normalized bending angles on time for bending actuators with $n = 2{:}2.5$, 2:3, and 2:3.5. (b) Dependence of the normalized twisting angle on time for twisting actuators with $\alpha = 30°, 45°$, and $60°$.

different actuators. The sinusoidal pressure can be written as

$$P_r = \frac{A}{2}\sin\left(2\pi f t - \frac{\pi}{2}\right) + \frac{A}{2} \tag{31}$$

where the amplitude $A = 40$ kPa. The frequency f is set as 0.3, 0.5, or 0.7 Hz. Each step is tested for 10 cycles. Without loss of generality, we used a bending actuator ($n = 2{:}3$) and twisting actuator ($\alpha = 30°$) as examples. Fig. 8(a) and (b) shows the hysteresis loops under different frequencies. It can be seen that the area enclosed by the hysteresis curves increases with the frequency, which means that the viscoelastic hysteresis nonlinearity is rate-dependent. We also compare the hysteresis loops of the actuators with different geometric parameters when the amplitude and frequency of the exciting pressure were 40 kPa

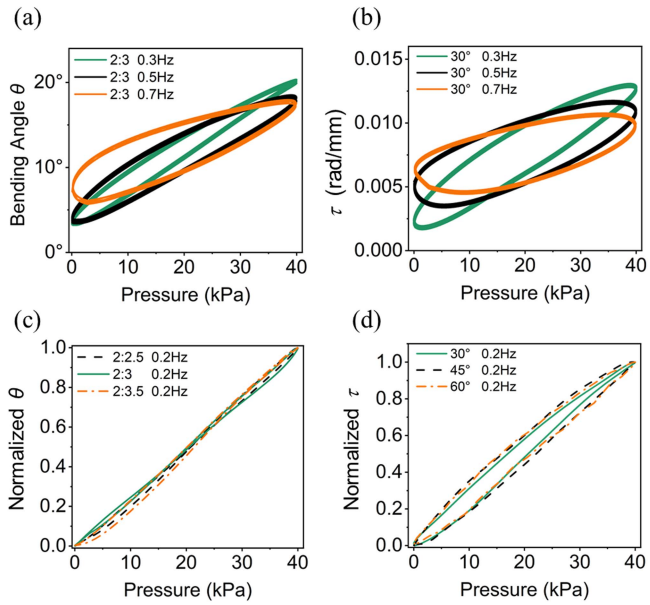

Fig. 8. Repeatability and loading-unloading loops. Loading and unloading loops of (a) bending soft actuators with a width ratio $n = 2{:}3$ and (b) twisting soft actuators with $\alpha = 30°$. Frequency of the applied pressure varies from 0.3 to 0.7 Hz. 10 cycles are shown for each test. Loading and unloading loops of (c) bending soft actuators with varying n and (d) twisting soft actuators with varying α under a pressure with 0.2 Hz.

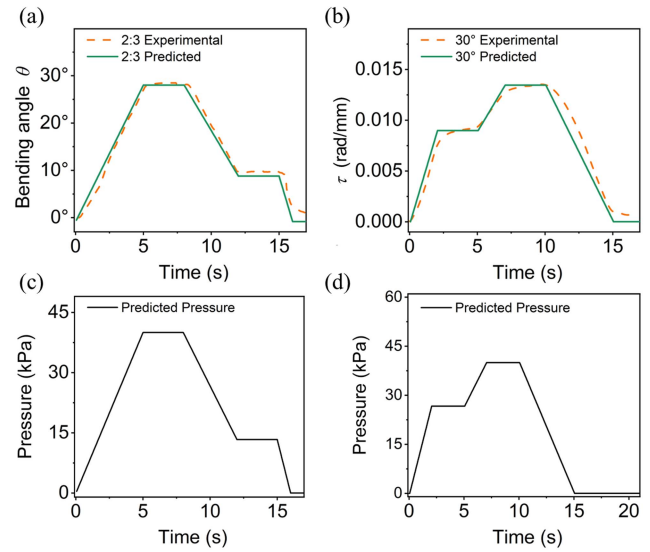

Fig. 9. Controllability tests. (a) Comparison of the model predicted and experimental bending angle θ for a bending soft actuators with $n = 2{:}3$. (b) Comparison of the model predicted and experimental twisting angle τ for a twisting soft actuator with $\alpha = 30°$. (c) and (d) Applied pressures during the bending and twisting controllability experiments, respectively.

and 0.2 Hz, respectively. Fig. 8(c) and (d) shows the normalized hysteresis loops with different n or α. The effects of geometric parameters on the hysteresis loops is relatively small.

The controllability of the soft actuators is tested. Fig. 9(a) compares the model predicted and experimental bending angle θ for a bending soft actuators with $n = 2{:}3$. Fig. 9(b) shows the model predicted and experimental twisting angle τ for a twisting soft actuator with $\alpha = 30°$. The applied pressures are shown in

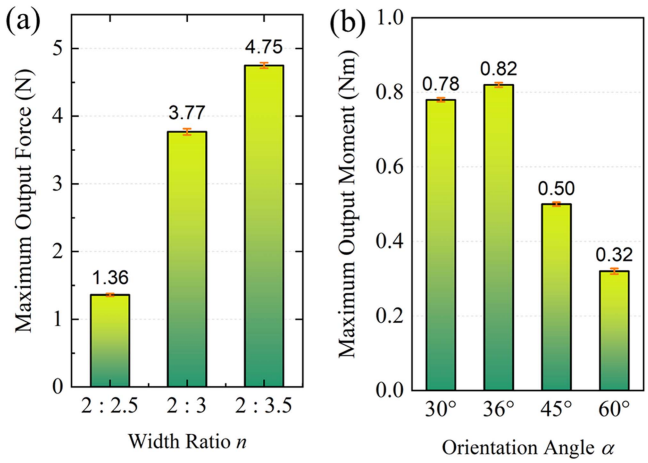

Fig. 10. Forces and torques of the actuators. (a) Maximum output bending force of bending soft actuators with different width ratio $n = 2{:}2.5$, 2:3, and 2:3.5. (b) Maximum output moment of twisting soft actuators with $\alpha = 30°$, 36°, 45°, and 60°. Ten tests are conducted for each soft actuator.

Fig. 9(c) and (d). The predicted θ and τ are calculated based on the validated theoretical model. Both the experimental and theoretical predicted θ and τ agree well, showing that the soft actuators are controllable.

The actuation force is an important factor in the soft actuator's performance [23], [32]. The blocking force of the bending soft actuator is measured using the experimental platform in Fig. 3(b). Fig. 10(a) shows the maximum output bending force of bending soft actuator with different width ratio $n = 2{:}2.5$, 2:3, and 2:3.5. The output force increases when the width ratio increases. The highest output force of the bending actuators is 4.75 N when the width ratio n is 2:3.5.

The output torque of the twisting soft actuator is measured using the axially rotatable force-measuring platform [see Fig. 3(c)]. As shown in Fig. 10(b), we investigated four different twisting actuators whose orientation angles $\alpha = 30°$, 36°, 45°, and 60°. The output moment tests show that the torque reaches the peak value 0.82 Nm when $\alpha = 36°$, agreeing with the theoretical and experimental results that the twisting soft actuator with $\alpha = \sim 36°$ shows the largest twisting angle shown in Figs. 5(k) and 6.

The dynamics behaviors of the bending and twisting soft actuators under a step pressure are studied. Fig. 11(a) shows the step response of a twisting soft actuator with $\alpha = 30°$ under step pressures 20, 30, or 40 kPa. The twisting angle increases with time and reaches its stable value due to the viscoelasticity of the silicone rubbers. The time taken for the twisting soft actuator to reach 80% of the stable τ is almost 0.7 s under the three different pressures. Fig. 11(b) shows the step response of three different twisting soft actuators with $\alpha = 30°$, 45°, and 60° under a step pressure with 40 kPa. The settling time with $\alpha = 60°$ is the lowest, while that with $\alpha = 30°$ is the highest, as the axial strain of the soft actuator with $\alpha = 30°$ is the largest. Similar tests were also conducted for the bending actuators under different pressures and width ratios, as shown in Fig. 11(c) and (d).

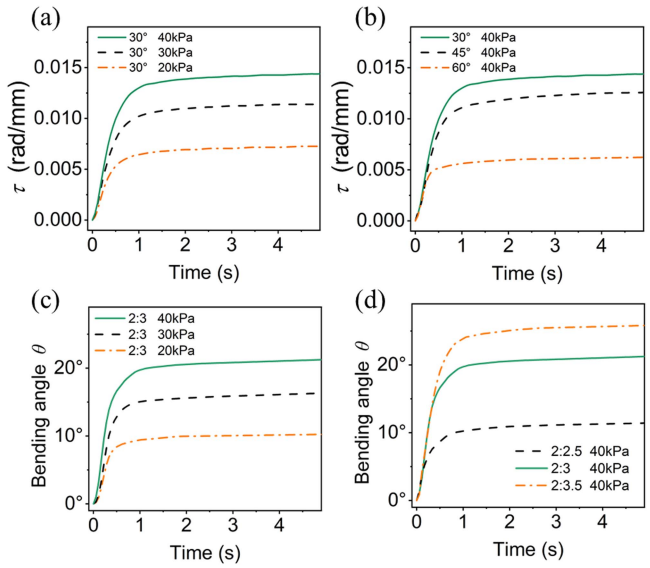

Fig. 11. Speed performances. (a) Step response of the twisting soft actuator with $\alpha = 30^\circ$ under a pressure with 20, 30, or 40 kPa. (b) Step response of the twisting soft actuator with different $\alpha = 30^\circ$, 45°, and 60° under a 40 kPa pressure. (c) Step response of a bending soft actuator with $n = 2{:}3$ under a pressure with 20, 30, or 40 kPa. (d) Step response of the bending soft actuator with different $n = 2{:}2.5$, 2:3, and 2:3.5 under a 40 kPa pressure.

VI. Numerical Results

As the theoretical model establishes the relationship between the input parameters and the deformed shapes, it can be applied to study the effect of the geometric, material and loading parameters on the motion of the soft actuators. In this section, various soft actuators are designed using the validated theory. The effects of geometric parameters (orientation angle and width ratio) are investigated.

A. Effects of Width Ratios and Inflation Pressure on Bending Soft Actuators

The theoretically predicted bending angle θ and axial strain λ_b are 3-D plotted as functions of P and width ratio n in Fig. 12(a) and (b). Both θ and λ_b increase with P. As the width of the thicker horseshoe increases, θ increases and λ_b decreases. The dependence of the bending angle θ on n is plotted under $P = 40$, 60, or 80 kPa in Fig. 12(c). θ increases rapidly and then reaches a plateau when the width ratio increases. The limit value of θ is $\sim 30^\circ$, $\sim 42^\circ$, and $\sim 51^\circ$, respectively. Fig. 12(d) shows the corresponding deformed shapes with different n. Fig. 12(e) plots the dependence of θ on P, for three different $n = 2{:}3$, 2:4, and 2:5. The theoretically predicted deformed shapes when $n = 2{:}4$ are shown in Fig. 12(f). θ changes from $\sim 14^\circ$ to $\sim 43^\circ$ when P increases from 20 to 100 kPa. Various shapes of the bending actuators can be formed by varying the width ratio and applied pressure.

B. Effects of Orientation Angles on Twisting Soft Actuator

Besides using only one set of tilted grids, multiple sets of tilted grids can also be used to tune the twisting and elongation performance of the twisting soft actuators resulting from the design freedom of the lattice structures. By adding the energy density part of the additional tilted grids in (5), the performance of the twisting soft actuators with multiple sets of tilted grids can be theoretically predicted. Detailed derivations of twisting soft actuators with two sets of tilted grids are shown in Appendix A. The performance of twisting soft actuators with more than two sets of tilted grids can be derived similarly.

Fig. 13(a) and (b) shows the dependence of the theoretically predicted twist per unit length τ and the axial strain λ_t on the orientation angle β when $\alpha = 30^\circ$ and $P = 40$ kPa. The orange dashed line shows the values of τ and λ_t when only a single tilted grid with $\alpha = 30^\circ$ is used. We have fabricated soft actuators with two sets of tilted grid $\alpha = 30^\circ$ and $\beta = 60^\circ$, 120°, or 150°. Fig. 13(c)–(e) shows the experimental results for the three soft actuators and the λ_t and τ are marked in Fig. 13(a) and (b), which match well with the theoretical prediction. Noted that the theoretical model cannot predict the deformation when α or β is small or equal to 180° (almost horizontal), as the deformation will violate the assumptions made.

VII. Applications

By adjusting the reinforced lattice, the pneumatic soft actuators can exhibit programmable bending, twisting, and elongation motions, enabling the design of soft robots with diverse functions. Based on the theoretical model, two soft robots are designed and demonstrated: lateral-climbing and exploration soft robots. By lattice superimposition, a soft actuator that exhibiting a combined bending, twisting, and elongation is demonstrated.

A. Lateral-Climbing Soft Robot

Many soft robots exhibit plane locomotion or vertical wall climbing abilities but lack the ability of lateral climbing, which could be potentially used to clean the exterior walls of tall buildings or geological exploration at the cliffs. Here, a lateral climbing soft robot is presented consisting of a two-segment soft actuator and two silicone suction feet. The two-segment soft actuator consists of two bending segments with $n = 2{:}3$ and 3:2 with independent input for each segment [see Fig. 14(a)]. The length of the soft actuator is 220 mm. The theoretical predicted deformed shapes are shown. The deformed shapes of the two-segment soft actuators are reconstructed by connecting the deformed shapes of each segment with coordinate transformation. It can be observed that the soft actuator exhibits an antisymmetric deformation with respect to its centers. By individually controlling the pressure in each segment, the top and bottom planes can remain parallel, compensating for the gravity effect.

Based on the theoretically predicted deformation, lateral climbing soft robots are designed. Silicone suction feet are assembled at both ends to provide suction forces. Two separate inputs are used to control the attachment (negative pressure) or release of the suction cups (positive pressure). By controlling the input pressure sequence, the locomotion of the soft robot can be controlled. A vertically placed acrylic plate is used as the surface for testing (is presented in Supplementary Video

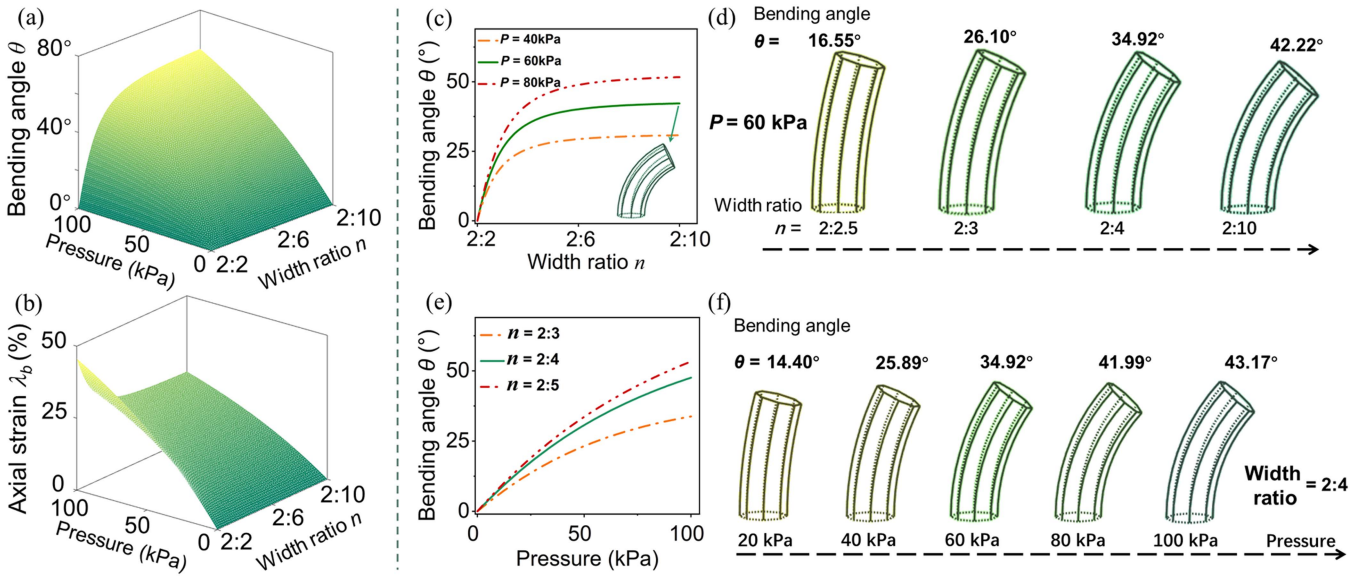

Fig. 12. Theoretical predicted effects of width ratio n and pressure P on bending soft actuators. (a) and (b) 3-D plot of the theoretically predicted bending angle θ and axial strain λ_b as functions of P and width ratio n. (c) Theoretically predicted dependence of θ on n at $P = 40$, 60, and 80 kPa. (d) Theoretically predicted deformed shapes at $n = 2{:}2.5$ to 2:10 with $P = 60$ kPa. (e) Theoretically predicted dependence of θ on P at $n = 2{:}3$ to 2:5. (f) Corresponding theoretically predicted deformed shapes.

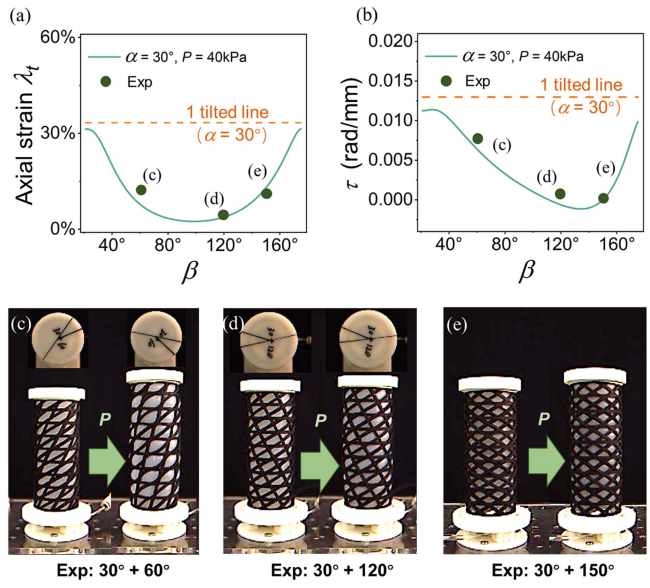

Fig. 13. Twisting soft actuators with two sets of tilted grids. (a) and (b) Theoretical predicted twisting per unit length τ and axial strain λ_t on the orientation angles α and β of the two sets of tilted grids. (c)–(e) Experimental results of the three soft actuators with $\alpha = 30°$ and $\beta = 60°$, 120°, or 150°.

S2). Fig. 14(b)–(h) shows the locomotion process in one cycle. Initially, the back foot is fixed while the front foot is released [see Fig. 14(c)]. As the inflation pressures of the two segments increase from 0 to 25 kPa and 32 kPa, the front foot moves laterally [see Fig. 14(d) and (e)]. Due to the antisymmetric deformation with respect to the central point, the top and bottom plane remains parallel. During deflation, the front foot is fixed while the bottom foot is released [see Fig. 14(f)]. The bottom foot moves laterally, and the soft robot returns to the vertical state [see Fig. 14(g)]. By repeating the above cycles, the soft robot moves laterally [see Fig. 14(h)].

B. Exploration Soft Manipulator

The dexterous motion of the lattice-reinforced soft actuators enables the design of soft robots for exploration. Here, an exploration soft manipulator is presented by assembling a two-segment soft actuator with a camera (see Fig. 15). The two-segment soft actuator consists of a bending segment ($n = 2{:}3.5$) and a twisting segment ($\alpha = 36°$). The length of both segments is 100 mm. Fig. 15(a) shows the theoretically predicted deformed shapes of the two-segment soft actuator. When inflated, the two-segment soft actuator exhibits a spatially combined twisting and bending trajectory. Each segment is controlled individually. In Fig. 15(b), each point represents the soft manipulator's top center. The applied pressure changes from 0 to 30 kPa for the bending part and 0 to 60 kPa for the twisting part. It rotates $\sim 185°$ with a maximum radius of 23 mm and a maximum height of 238 mm. The broad workspace enables the design of the exploration soft manipulator.

An eight prism box with no lid is made to simulate a cave environment. Eight letters 'SJTUSORO' are printed on the barrel walls [see Fig. 15(d)]. The soft manipulator reaches out from the bottom hole of the box, and the camera film the inside to exhibit the exploration ability of the soft robot. Fig. 15(e) shows the pictures captured by the camera as the actuated pressure P increases. It can be observed that the manipulator sweeps more than 180° when P is around 60 kPa. The vision taken from the camera covers more than 270°, and six letters out of eight are captured. The possible application scenarios include navigating tight spaces and inspection. The soft manipulator's ability to bend and twist allows it to navigate through tight spaces, crevices, and debris. Equipped with a camera, the soft

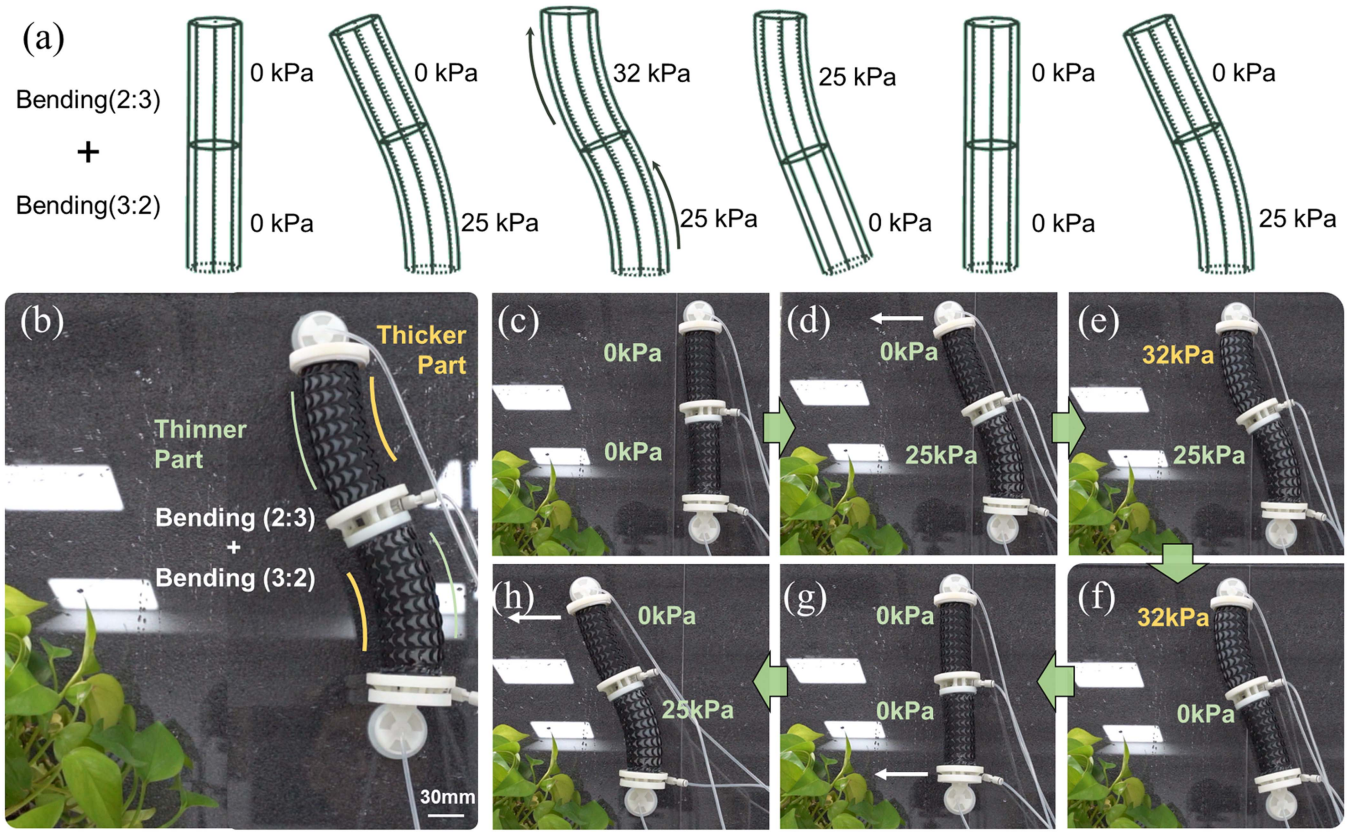

Fig. 14. Lateral-climbing soft robot is designed consisting of a two-inputs soft actuator and two silicone suction feet. (a) Theoretically predicted antisymmetric deformation of soft actuators consists of two bending segments with $n = 3{:}2$ and 2:3. (b)–(h) Soft robot moves laterally on the vertical surface due to the periodical input pressures.

manipulator can explore the surroundings and provide real-time footage to rescuers.

C. Lattice Superimposition

One advantage of the lattice-reinforced soft actuator is that the geometric patterns can be superimposed, enabling the design of various combined deformations and dexterous motion in 3-D space. Bobbit worms, excellent predators in the sea, catch fishes swimming by using their bodies' complex 3-D motions. Inspired by the dexterous predation action, we have designed a soft actuator that demonstrates coupled elongation, twisting, and bending deformations within a single segment (is presented in Supplementary Video S2).

The reinforced lattice consists of tilted horseshoe structures with different width distribution, which contains all the elements for elongation, twisting, and bending [see Fig. 16(a)]. The large stretchability of the horseshoe structures enables an elongation deformation. The horseshoe structure is tilted by an angle $\alpha = 60^\circ$, leading to twisting deformation. The width of the horseshoe structures gradually changes from 2 to 4 mm $w_1 = 2$ mm, $w_2 = 3$ mm, and $w_3 = 4$ mm, resulting in a bending deformation. Horizontal rings are used to constrain the radial expansions. Fig. 16(b)–(e) shows the deformation of the twisting–bending–elongation coupled soft manipulators under $P = 10$ to 40 kPa.

The lattice employs a pattern that superimposes three different design methods, which enables the soft actuator to exhibit combined twisting, bending, and elongation motions. Achieving multiple deformations using a single segment is an active research area in soft robotics. Examples include bubble casting soft robots harnessing interfacial flows [46], programmable three-chambered soft actuator modules [47], and reconfigurable soft robots based on origami artificial muscles [48]. The ability to achieve complex motions by pattern superimposition in lattice design is an advantage of this work, which may open up possibilities for more complex and diverse applications in soft robotics. Note that the soft actuator exhibits a spatial trajectory, which is challenging to model accurately. We recognize this as an area for future exploration and improvement.

VIII. Discussion and Conclusion

The complex patterns in the reinforced lattice layer enable the formation of controllable deformations through anisotropy, which is essential for a soft actuator to perform a particular motion or a target application and has attracted significant progress recently. The design method, coupled with optimization algorithms, can generate diverse 3-D trajectories. These capabilities have the potential for real-world applications in seafood animal collections, vegetable and fruit harvesting, soft prosthetics, confined space operations, hazardous environment

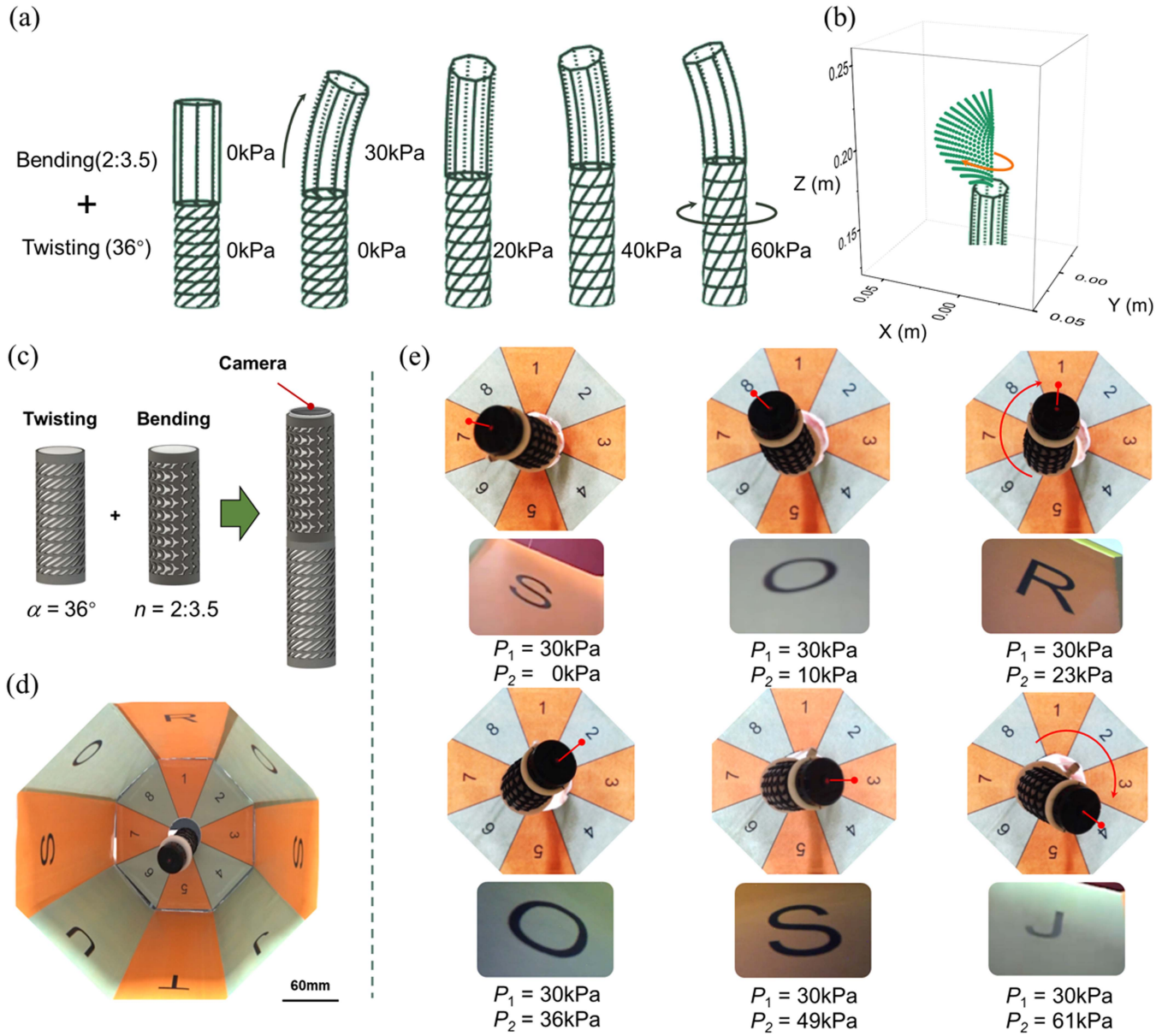

Fig. 15. Exploration soft manipulator. (a) Soft actuator consisting of a bending segment (n = 2:3.5) and a twisting segment ($\alpha = 36°$) exhibits a spatially combined twisting and bending trajectory when inflated. (b) Green points show the trajectory of the manipulator's top end. (c) Exploration soft manipulator consists of a two-segment soft actuator and a camera. (d) Simulated cave environment using an eight prism box with no lid. (e) Soft manipulator sweeps more than 180° when P_2 is around 61 kPa. In total, six letters out of eight are captured by the camera.

tasks, delicate soft manipulators matching the surface of fragile objects, and the development of bio-inspired soft robots, such as mimicking octopus tentacles' versatile grasping.

Motion decoupling could facilitate the formation of complex trajectories using modular assembly. Soft actuators often exhibit coupled deformation, making motion decoupling a complex task. Decoupling is particularly challenging in pneumatic soft actuators, as air pressure will inevitably lead to expansion in both radial and axial directions. Various soft actuators in the literature have demonstrated coupled deformation with axial elongation and radial expansion, such as the origami-inspired twisting soft actuator powered by vacuum [49], twisting soft actuators by freeform surface design [50], twisting soft actuator for wall climbing robot [51], and twisted and coiled soft actuators [52].

In this work, achieving independent twisting deformation by pattern design is difficult, as the twisting and bending deformation is induced by the axial elongation. One possible way to generate twisting without elongation deformation could be by releasing the circular constraint and adjusting the orientation angle. As shown in [31] and [53], the axial elongation can reduce or even change to contraction by allowing radial expansion and adjusting the orientation angle. However, this method still involves the coupling of twisting and radial expansion. An alternative way to achieve independent twisting deformation could involve designing the grid as tubes and applying air pressure to

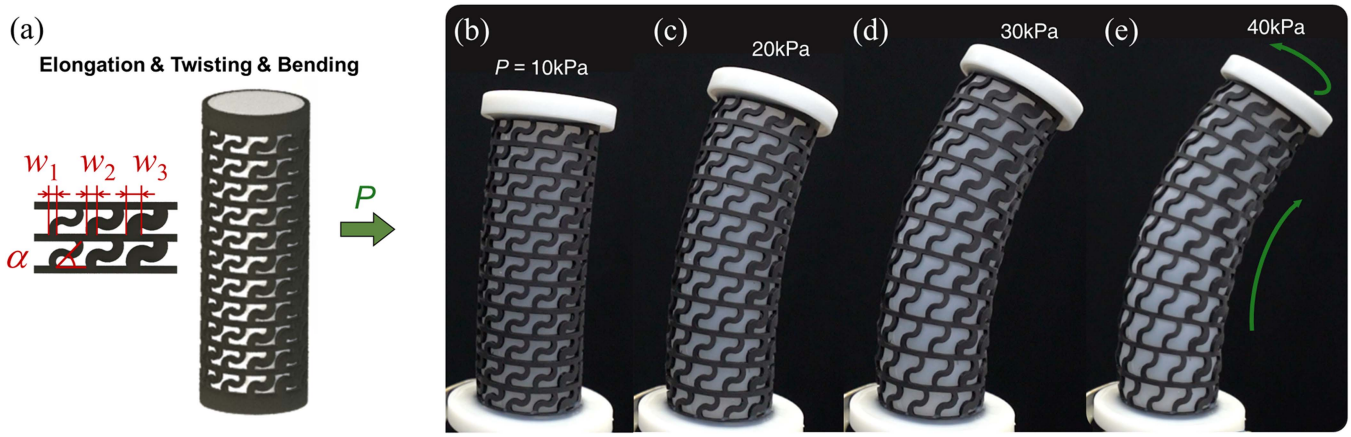

Fig. 16. Lattice superimposition. (a) Reinforced lattice consists of tilted horseshoe structures with different width distributions, enabling coupled elongation-twisting-bending deformations during inflation (b)–(e).

them rather than relying on inner axial pressure, which might allow for more control over twisting. Further research is required to decouple these motions fully.

We have effectively mitigated the bulging effect using a thick inner silicone tube and narrow grid spacings. However, the bulging effect remains significant and cannot be neglected when dealing with lattice designs that feature thin inner silicone tubes or large gaps. The developed theoretical model can only work without consideration of the bulging effect. Bulging is an inherent localized instability, and future research is necessary to explore and address the bulging effect.

The design method of using lattice layers to control the deformation of soft actuators has previously been proposed by Pan et al. [43], which focuses on the design optimization of bending soft actuators by a combination of experiments and FE simulations. Inspired by [43], this work has extended the bending deformation to all twisting, bending, and elongation deformations and developed a theoretical framework to predict the deformation, which widens the design space and enables the design of complex trajectories for applications. This work presents pneumatic lattice metamaterial reinforced soft actuators that exhibit programmable bending, twisting, and elongation deformations. We develop a nonlinear theoretical framework to predict finite deformation. An orthotropic nonlinear energy density function is used to describe the twisting soft actuators. Their twisting, expansion, and elongation are obtained by solving the Cauchy equilibrium equations in cylindrical coordinates. A bending model taking into account the nonlinear stress-strain curves of the horseshoe microstructures is developed. The elongation soft actuators are modeled as a particular case of the bending model with uniform widths. The effects of orientation angles, geometric patterns, and thickness ratios are studied using the validated theoretical model. Theoretical guided designs of lateral-climbing soft robots and exploration soft manipulators are demonstrated.

The major contributions and findings can be summarized as follows. First, we propose the design method using lattice structures to control pneumatic soft actuators' twisting, bending, and elongation deformation. Second, we develop a nonlinear theoretical framework to program the deformations, which is validated by experiments. Third, numerical results are conducted to study the effects of orientation angles, geometric patterns and the number of tilted grids. Results show that the twisting is maximized when the tilted angle is around 36°, while the soft actuators exhibit pure elongation when the tilted angle of two grids is supplementary. Finally, soft robots are designed based on the theoretical model: a lateral-climbing soft robot with S-shaped deformation and an exploration soft robot with programmable trajectories. The proposed structural design method paves the way for designing soft robots with complex and dexterous deformations.

Appendix A

A Modeling of Twisting Soft Actuators With Multiple Sets of Tilted Grids

The twisting soft actuators with multiple sets of tilted grids are modeled in this section. The lattice-reinforced twisting actuator consists of the internal silicone cylinder and the outer rubber skeleton. The inner layer is isotropic, while the outer layer is anisotropic due to the circular and tilted grids. For the two-set tilted grids twisting actuator, the energy density function is

$$\begin{aligned} W_t^{(\text{aniso})} &= \frac{(\sqrt{\mathbf{I}_4}-1)^2 E_t}{2} + \frac{(\sqrt{\mathbf{I}_6}-1)^2 E_t}{2} + \frac{k_{t1}{\theta_{t1}}^2}{2V_1} \\ &\quad + \frac{(\sqrt{\mathbf{I}_{10}}-1)^2 E_t}{2} + \frac{k_{t2}{\theta_{t2}}^2}{2V_2} \end{aligned} \tag{A1}$$

where $\frac{k_{t1}{\theta_{t1}}^2}{2V_1}$ and $\frac{k_{t2}{\theta_{t2}}^2}{2V_2}$ are the bending energy density of the two sets of grids, separately. $\boldsymbol{I}_{10} = \boldsymbol{F}\boldsymbol{A_3} \cdot \boldsymbol{F}\boldsymbol{A_3}$ are pseudoinvariant of the second tilted grid. $\boldsymbol{A}_3 = (0, \cos\alpha_2, \sin\alpha_2)$ is the direction of the tilted lattice in the undeformed configuration. Then, the Cauchy stresses can be obtained as

$$\boldsymbol{\sigma} = 2\frac{\partial W_t}{\partial I_1}\boldsymbol{B} + 2\frac{\partial W_t}{\partial I_4}\mathbf{s}_1 \otimes \boldsymbol{s}_1 + 2\frac{\partial W_t}{\partial I_6}\boldsymbol{s}_2 \otimes \boldsymbol{s}_2$$

$$+2\frac{\partial W_t}{\partial I_{10}}\boldsymbol{s}_3\otimes\boldsymbol{s}_3-p\boldsymbol{I}. \tag{A2}$$

The Cauchy stress can be written explicitly as

$$\sigma=\begin{pmatrix}\sigma_{rr}&0&0\\0&\sigma_{\theta\theta}&\sigma_{\theta z}\\0&\sigma_{z\theta}&\sigma_{zz}\end{pmatrix} \tag{A3}$$

where

$$\sigma_{rr}=-P+\frac{c_1\mu}{{\lambda_t}^2{\lambda_\theta}^2} \tag{A4}$$

$$\sigma_{\theta\theta}=-P+c_1(\gamma^2{\lambda_t}^2+{\lambda_\theta}^2)\mu + \begin{pmatrix}\frac{c_2E(-1+\sqrt{I_6})\lambda_\theta{}^2}{\sqrt{I_6}}+\frac{c_2E(-1+\sqrt{I_4})(\lambda_\theta\cos\alpha+\gamma\lambda_t\sin\alpha)^2}{\sqrt{I_4}}\\+\frac{c_2E(-1+\sqrt{I_{10}})(\lambda_\theta\cos\alpha_2+\gamma\lambda_t\sin\alpha_2)^2}{\sqrt{I_{10}}}\end{pmatrix} \tag{A5}$$

$$\sigma_{zz}=-P+c_1{\lambda_t}^2\mu + \frac{c_2E(-1+\sqrt{I_4})\lambda_t{}^2\sin^2\alpha}{\sqrt{I_4}}+\frac{c_2E(-1+\sqrt{I_{10}})\lambda_t{}^2\sin^2\alpha_2}{\sqrt{I_{10}}} \tag{A6}$$

$$\sigma_{\theta z}=\sigma_{z\theta} = \lambda_t\begin{pmatrix}c_1\gamma\lambda_t\mu+\frac{c_2E(-1+\sqrt{I_4})\sin\alpha(\lambda_\theta\cos\alpha+\gamma\lambda_t\sin\alpha)}{\sqrt{I_4}}\\+\frac{c_2E(-1+\sqrt{I_{10}})\sin\alpha_2(\lambda_\theta\cos\alpha_2+\gamma\lambda_t\sin\alpha_2)}{\sqrt{I_{10}}}\end{pmatrix}. \tag{A7}$$

The three boundary conditions are as follows.

BC1:

$$P=\int_{r_i}^{r_o}\left(\lambda_\theta\frac{\partial W_t}{\partial\lambda_\theta}+\gamma\frac{\partial W_t}{\partial\gamma}\right)\frac{dr}{r}. \tag{A8}$$

BC2:

$$N=\pi\int_{r_i}^{r_o}\left(2\lambda_t\frac{\partial W_t}{\partial\lambda_t}-\lambda_\theta\frac{\partial W_t}{\partial\lambda_\theta}-3\gamma\frac{\partial W_t}{\partial\gamma}\right)rdr+P\pi r_i^2. \tag{A9}$$

BC3:

$$M=2\pi\int_{r_i}^{r_o}\frac{\partial W_t}{\partial\gamma}r^2dr. \tag{A10}$$

By using the above boundary conditions, the three parameters τ, λ_t, and P can be solved numerically.

B Stress Terms in (10)

The Cauchy stress can then be written explicitly in the matrix form

$$\sigma=\begin{pmatrix}\sigma_{rr}&0&0\\0&\sigma_{\theta\theta}&\sigma_{\theta z}\\0&\sigma_{z\theta}&\sigma_{zz}\end{pmatrix} \tag{A11}$$

where

$$\sigma_{rr}=-p+\frac{c_1\mu}{{\lambda_t}^2{\lambda_\theta}^2} \tag{A12}$$

$$\sigma_{\theta\theta}=-p+c_1(\gamma^2{\lambda_t}^2+{\lambda_\theta}^2)\mu+\frac{c_2E(-1+\sqrt{I_6})\lambda_\theta{}^2}{\sqrt{I_6}} + \frac{c_2E(-1+\sqrt{I_4})(\lambda_\theta\cos\alpha+\gamma\lambda_t\sin\alpha)^2}{\sqrt{I_4}} \tag{A13}$$

$$\sigma_{zz}=-p+c_1{\lambda_t}^2\mu+\frac{c_2E(-1+\sqrt{I_4})\lambda_t{}^2\sin^2\alpha}{\sqrt{I_4}} \tag{A14}$$

$$\sigma_{\theta z}=\sigma_{z\theta}=\lambda_t\begin{pmatrix}c_1\gamma\lambda_t\mu\\+\frac{c_2E(-1+\sqrt{I_4})\sin\alpha(\lambda_\theta\cos\alpha+\gamma\lambda_t\sin\alpha)}{\sqrt{I_4}}\end{pmatrix} \tag{A15}$$

and $\gamma=\tau r$.

Geometrical and Material Parameters for Lattice-reinforced Actuators				
L_0 (mm)	85			
R_i (mm)	16			
R_o (mm)	18			
Number of circular restrictions	8			
Thickness of the rubber skeleton	2 mm			
Thickness of the silicone liner	4 mm			
Twisting Actuators				
Parameters	$\alpha=30°$	$\alpha=36°$	$\alpha=45°$	$\alpha=60°$
Number of columns	20			
Tilted angle α (°)	30	36	45	60
Bending(Elongation) Actuators				
Parameters	$n=2{:}2$	$n=2{:}2.5$	$n=2{:}3$	$n=2{:}3.5$
w_1 (mm)	2			
w_2 (mm)	2	2.5	3	3.5
Thinner columns	15	8	8	8
Thicker columns	0	8	8	7
Material	E (Mpa)		v	
Ecoflex 00-50	0.082		0.499	
Rubber lattice	19.2		0.499	

Fig. 17. Geometrical and material parameters for lattice metamaterial reinforced Actuators.

C Force and Strain Relationship of Horseshoe Structures

Consider a horseshoe microstructure with thickness h and width w simply supported and deformed under horizontal force f at each end [see Fig. 2(g)]. Using the force and moment balances, the governing equation of the basic curve can be written as [37]

$$\frac{d^2\theta_h}{d\alpha_h^2}=\frac{R_h^2\cdot(f\sin\theta_h)\cdot(EA_h+f\cos\theta_h)}{EI_h\cdot EA_h} \tag{A16}$$

where $\theta_h(\theta_h^0\le\theta_h\le\theta_h^{\text{end}})$ and α_h are the deformed and undeformed slope angles, $A_h=w\times h$ the cross-section area of the horseshoe microstructure and $I_h(I_h=w^3h/12)$ is the second area moment.

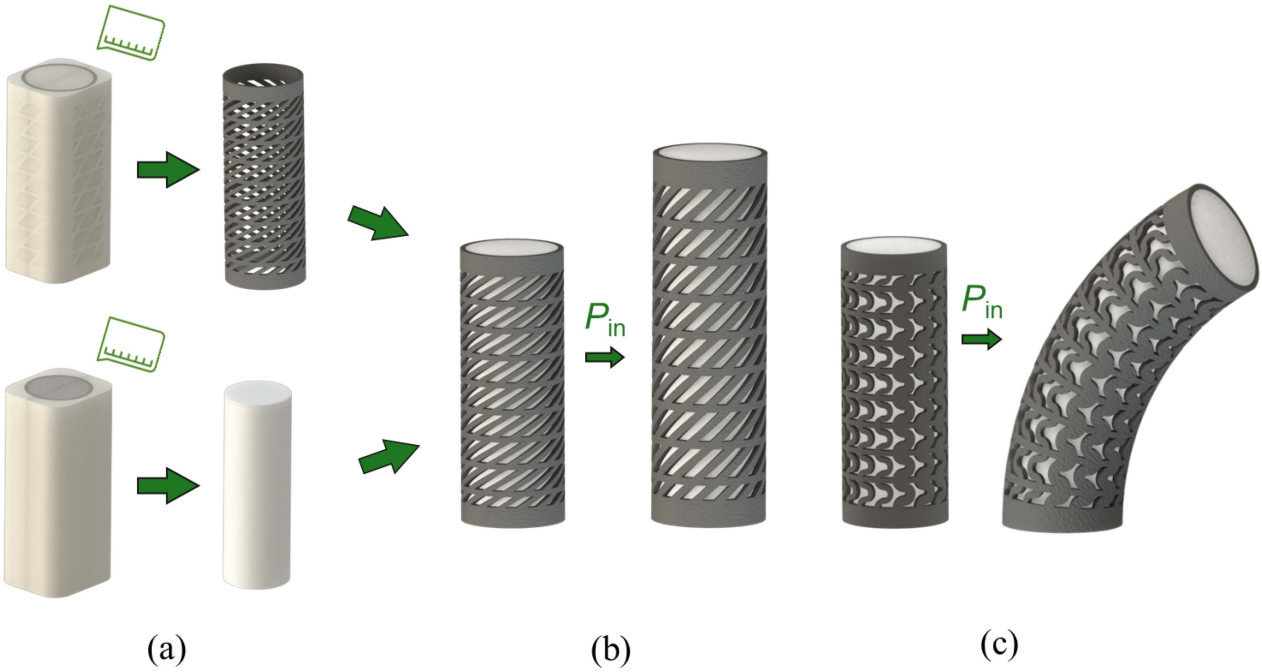

Fig. 18. Fabrication procedures of lattice-reinforced soft actuators. (a) Outer lattice structures and the inner silicone are obtained by molding. (b) Reinforced lattice of the twisting soft actuator consists of a set of tilted grids and a set of circular grids. (c) Reinforced lattice of the bending soft actuator consists of horseshoe lattices with different widths and a set of circular grids.

Equation (A16) is a second-order ordinary differential equation of θ_h and can be solved using the following two boundary conditions:

(BC4)

$$\frac{d\theta_h}{d\alpha_h}(\alpha_h = 0) = 1. \tag{A17}$$

(BC5)

$$\int \sin\theta_h ds = 0. \tag{A18}$$

The x and y coordinates of deformed microstructure can be calculated by integrations. Hence, we can write the force-strain relationship as a function of the axial strain ε and width w as

$$f = f(\varepsilon, w). \tag{A19}$$

D Manufacturing Parameters of the Lattice Reinforced Actuators

The manufacturing parameters of the lattice reinforced soft actuators are given in Fig. 17.

E Fabrication Procedures

The fabrication procedures of the lattice-reinforced actuators are shown in Fig. 18. Both the outer lattice structures and inner silicone are fabricated by molding. The manufacturing process of the lattice structure uses a replication technique. The structure is designed using SolidWorks (Dassault Systèmes SOLIDWORKS Corp) and then 3-D printed. A mold of the the lattice structure is created by the casting process. The commercially available polyurethane-based rubber, Hei-Cast 8400 (Shore 90 A) (Wenext, Shenzhen) is then used to fabricate the lattice structure using the mold. The two ends of both structures are glued together. The pressure is applied from one end using an air pump.

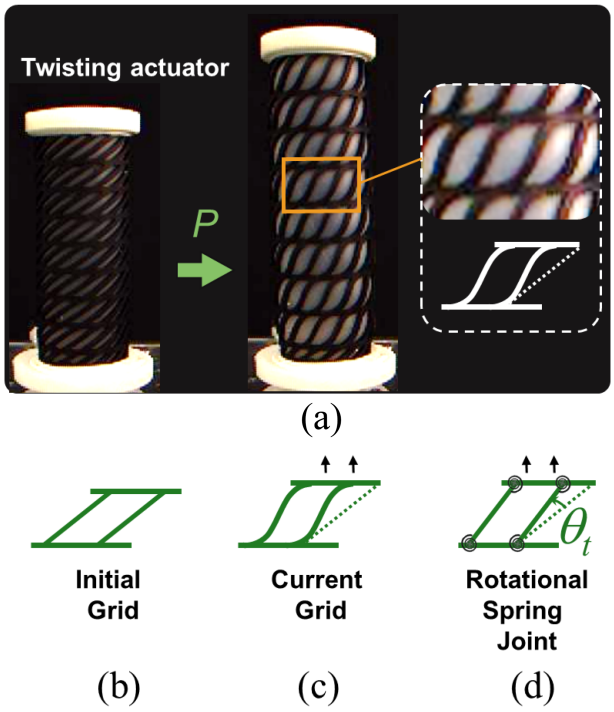

Fig. 19. (a) Tilted grids bend at the joints of the tilted and circular grids during actuation. (b) Initial configuration. (c) Current configuration. (d) Rotational spring joint to approximate the bending.

F Bending Energy of the Grid Unit

Fig. 19 shows the deformation of the grid unit. The deformation of the grid unit consists of both elongation and bending. The bending is modeled as rotational spring joint with a bending angle θ_t.

References

[1] C. Laschi, B. Mazzolai, and M. Cianchetti, "Soft robotics: Technologies and systems pushing the boundaries of robot abilities," *Sci. Robot.*, vol. 1, no. 1, 2016, Art. no. eaah3690.

[2] A. Rajappan, B. Jumet, and D. J. Preston, "Pneumatic soft robots take a step toward autonomy," *Sci. Robot.*, vol. 6, no. 51, 2021, Art. no. eabg6994.

[3] D. Rus and M. T. Tolley, "Design, fabrication and control of soft robots," *Nature*, vol. 521, no. 7553, pp. 467–475, 2015.

[4] V. Sundaram et al., "Embedded magnetic sensing for feedback control of soft HASEL actuators," *IEEE Trans. Robot.*, vol. 39, no. 1, pp. 808–822, Feb. 2023.

[5] M. F. Simons et al., "B: Ionic glove: A soft smart wearable sensory feedback device for upper limb robotic prostheses," *IEEE Robot. Automat. Lett.*, vol. 6, no. 2, pp. 3311–3316, Apr. 2021.

[6] M. Lin, H. Hu, S. Zhou, and S. Xu, "Soft wearable devices for deep-tissue sensing," *Nature Rev. Mater.*, vol. 7, pp. 1–20, 2022.

[7] C. S. Xian et al., "Locomotion of miniature soft robots," *Adv. Mater.*, vol. 33, no. 19, 2021, Art. no. 2003558.

[8] Z. Zhang et al., "Pneumatically controlled reconfigurable bistable bionic flower for robotic gripper," *Soft Robot.*, vol. 9, no. 4, pp. 657–668, 2022.

[9] K. Ly, J. V. Mayekar, S. Aguasvivas, C. Keplinger, M. E. Rentschler, and N. Correll, "Electro-hydraulic rolling soft wheel: Design, hybrid dynamic modeling, and model predictive control," *IEEE Trans. Robot.*, vol. 38, no. 5, pp. 3044–3063, Oct. 2022.

[10] Y. Li et al., "A dual-mode actuator for soft robotic hand," *IEEE Robot. Automat. Lett.*, vol. 6, no. 2, pp. 1144–1151, Apr. 2021.

[11] C. Tawk and G. Alici, "A review of 3 D printable soft pneumatic actuators and sensors: Research challenges and opportunities," *Adv. Intell. Syst.*, vol. 3, no. 6, 2021, Art. no. 2000223.

[12] Z. Wang and S. Hirai, "Analytical modeling of a soft pneu-net actuator subjected to planar tip contact," *IEEE Trans. Robot.*, vol. 38, no. 5, pp. 2720–2733, Oct. 2022.

[13] D. Bruder, X. Fu, R. B. Gillespie, C. D. Remy, and R. Vasudevan, "Data-driven control of soft robots using Koopman operator theory," *IEEE Trans. Robot.*, vol. 37, no. 3, pp. 948–961, Jun. 2021.

[14] O. Goury and C. Duriez, "Fast, generic, and reliable control and simulation of soft robots using model order reduction," *IEEE Trans. Robot.*, vol. 34, no. 6, pp. 1565–1576, Dec. 2018.

[15] C. M. Best, L. Rupert, and M. D. Killpack, "Comparing model-based control methods for simultaneous stiffness and position control of inflatable soft robots," *Int. J. Robot. Res.*, vol. 40, no. 1, pp. 470–493, 2021.

[16] D. Wang et al., "Effect of temperature on the programmable helical deformation of a reconfigurable anisotropic soft actuator," *Int. J. Solids Structures*, vol. 199, pp. 169–180, 2020.

[17] G. Singh and G. Krishnan, "Designing fiber-reinforced soft actuators for planar curvilinear shape matching," *Soft Robot.*, vol. 7, no. 1, pp. 109–121, 2020.

[18] Y. Sang et al., "Reconfigurable soft body trajectories using unidirectionally stretchable composite laminae," *Nature Commun.*, vol. 10, no. 1, pp. 1–8, 2019.

[19] Y. Cui, X.-J. Liu, X. Dong, J. Zhou, and H. Zhao, "Enhancing the universality of a pneumatic gripper via continuously adjustable initial grasp postures," *IEEE Trans. Robot.*, vol. 37, no. 5, pp. 1604–1618, Oct. 2021.

[20] Y. Hao et al., "A multimodal, enveloping soft gripper: Shape conformation, bioinspired adhesion, and expansion-driven suction," *IEEE Trans. Robot.*, vol. 37, no. 2, pp. 350–362, Apr. 2021.

[21] F. Stella, N. Obayashi, C. D. Santina, and J. Hughes, "An experimental validation of the polynomial curvature model: Identification and optimal control of a soft underwater tentacle," *IEEE Robot. Automat. Lett.*, vol. 7, no. 4, pp. 11410–11417, Oct. 2022.

[22] L. Ge et al., "Design, modeling, and evaluation of fabric-based pneumatic actuators for soft wearable assistive gloves," *Soft Robot.*, vol. 7, no. 5, pp. 583–596, 2020.

[23] W. Hu and G. Alici, "Bioinspired three-dimensional-printed helical soft pneumatic actuators and their characterization," *Soft Robot.*, vol. 7, no. 3, pp. 267–282, 2020.

[24] K. M. de Payrebrune and O. M. O'Reilly, "On constitutive relations for a rod-based model of a pneu-net bending actuator," *Extreme Mechanics Lett.*, vol. 8, pp. 38–46, 2016.

[25] C. Jiang, D. Wang, B. Zhao, Z. Liao, and G. Gu, "Modeling and inverse design of bio-inspired multi-segment pneu-net soft manipulators for 3 D trajectory motion," *Appl. Phys. Rev.*, vol. 8, no. 4, 2021, Art. no. 041416.

[26] T. L. Buckner, R. A. Bilodeau, S. Y. Kim, and R. Kramer-Bottiglio, "Roboticizing fabric by integrating functional fibers," *Proc. Nat. Acad. Sci.*, vol. 117, no. 41, pp. 25360–25369, 2020.

[27] K. G. Klute and B. Hannaford, "Accounting for elastic energy storage in McKibben artificial muscle actuators," *J. Dyn. Sys., Meas., Control*, vol. 122, no. 2, pp. 386–388, 2000.

[28] B. Tondu, "Modeling of the Mckibben artificial muscle: A review," *J. Intell. Mater. Syst. Structures*, vol. 23, no. 3, pp. 225–253, 2012.

[29] P. Polygerinos et al., "Modeling of soft fiber-reinforced bending actuators," *IEEE Trans. Robot.*, vol. 31, no. 3, pp. 778–789, Jun. 2015.

[30] J. Bishop-Moser and S. Kota, "Design and modeling of generalized fiber-reinforced pneumatic soft actuators," *IEEE Trans. Robot.*, vol. 31, no. 3, pp. 536–545, Jun. 2015.

[31] F. Connolly, C. J. Walsh, and K. Bertoldi, "Automatic design of fiber-reinforced soft actuators for trajectory matching," in *Proc. Nat. Acad. Sci.*, vol. 114, no. 1, pp. 51–56, 2017.

[32] Q. Guan, J. Sun, Y. Liu, N. M. Wereley, and J. Leng, "Novel bending and helical extensile/contractile pneumatic artificial muscles inspired by elephant trunk," *Soft Robot.*, vol. 7, no. 5, pp. 597–614, 2020.

[33] D. S. Shah, E. J. Yang, M. C. Yuen, E. C. Huang, and R. KramerBottiglio, "Jamming skins that control system rigidity from the surface," *Adv. Funct. Mater.*, vol. 31, no. 1, 2021, Art. no. 2006915.

[34] V. Ramses, C. R. Martinez, X. F. Chen, and G. M. Whitesides, "Elastomeric origami: Programmable paper-elastomer composites as pneumatic actuators," *Adv. Funct. Mater.*, vol. 22, no. 7, pp. 1376–1384, 2012.

[35] L. Belding et al., "Slit tubes for semisoft pneumatic actuators," *Adv. Mater.*, vol. 30, no. 9, 2018, Art. no. 1704446.

[36] J. T. Overvelde, T. Kloek, J. J. D'haen, and K. Bertoldi, "Amplifying the response of soft actuators by harnessing snap-through instabilities," in *Proc. Nat. Acad. Sci.*, vol. 112, no. 35, pp. 10863–10868, 2015.

[37] L. Dong et al., "Modeling and design of periodic polygonal lattices constructed from microstructures with varying curvatures," *Phys. Rev. Appl.*, vol. 17, no. 4, 2022, Art. no. 044032.

[38] Y. Chen, T. Li, F. Scarpa, and L. Wang, "Lattice metamaterials with mechanically tunable Poisson's ratio for vibration control," *Phys. Rev. Appl.*, vol. 7, no. 2, 2017, Art. no. 024012.

[39] S. Yuan et al., "3 D soft auxetic lattice structures fabricated by selective laser sintering: TPU powder evaluation and process optimization," *Mater. Des.*, vol. 120, pp. 317–327, 2017.

[40] R. W. Ogden, *Non-Linear Elastic Deformations*. Mineola, NY, USA: Courier Corporation, 1997.

[41] Y. Zhang, K. Yu, K. H. Lee, K. Li, H. Du, and Q. Wang, "Mechanics of stretchy elastomer lattices," *J. Mechanics Phys. Solids*, vol. 159, 2022, Art. no. 104782.

[42] F. Kassianidis, "Boundary-value problems for transversely isotropic hyperelastic solids," Ph.D Dissertation, Univ. of Glasgow, Glasgow, Scotland, 2007.

[43] Q. Pan, S. T. Chen, F. F. Chen, and X. Y. Zhu, "Programmable soft bending actuators with auxetic metamaterials," *Sci. China Technol. Sci.*, vol. 63, no. 12, pp. 2518–2526, 2020.

[44] C. Horgan and J. Murphy, "Magic angles for fibrous incompressible elastic materials," in *Proc. Roy. Soc. A: Mathematical, Phys. Eng. Sci.*, vol. 474, no. 2211, 2018, Art. no. 20170728.

[45] C. Horgan and J. Murphy, "Magic angles and fibre stretch in arterial tissue: Insights from the linear theory," *J. Mech. Behav. Biomed. Mater.*, vol. 88, pp. 470–477, 2018.

[46] T. J. Jones, E. Jambon-Puillet, J. Marthelot, and P.-T. Brun, "Bubble casting soft robotics," *Nature*, vol. 599, no. 7884, pp. 229–233, 2021.

[47] J. Yan, H. Dong, X. Zhang, and J. Zhao, "A three-chambed soft actuator module with omnidirectional bending motion," in *Proc. IEEE Int. Conf. Real-Time Comput. Robot.*, 2016, pp. 505–510.

[48] Z. Jiao, C. Zhang, W. Wang, M. Pan, H. Yang, and J. Zou, "Advanced artificial muscle for flexible material-based reconfigurable soft robots," *Adv. Sci.*, vol. 6, no. 21, 2019, Art. no. 1901371.

[49] Z. Jiao, C. Ji, J. Zou, H. Yang, and M. Pan, "Vacuum-powered soft pneumatic twisting actuators to empower new capabilities for soft robots," *Adv. Mater. Technol.*, vol. 4, no. 1, 2019, Art. no. 1800429.

[50] F. Chen, Y. Miao, G. Gu, and X. Zhu, "Soft twisting pneumatic actuators enabled by freeform surface design," *IEEE Robot. Autom. Lett.*, vol. 6, no. 3, pp. 5253–5260, Jul. 2021.
[51] G. Chen, T. Lin, G. Lodewijks, and A. Ji, "Design of an active flexible spine for wall climbing robot using pneumatic soft actuators," *J. Bionic Eng.*, vol. 20, no. 2, pp. 530–542, 2023.
[52] S. Y. Yang et al., "High performance twisted and coiled soft actuator with spandex fiber for artificial muscles," *Smart Mater. Structures*, vol. 26, no. 10, 2017, Art. no. 105025.
[53] M. Schaffner, J. A. Faber, L. Pianegonda, P. A. Rühs, F. Coulter, and A. R. Studart, "3 D printing of robotic soft actuators with programmable bioinspired architectures," *Nature Commun.*, vol. 9, no. 1, 2018, Art. no. 878.

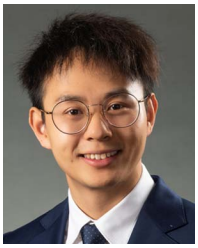

Dong Wang received the B.E. degree in mechanical engineering from Zhejiang University, Hangzhou, China, in 2010, and the Ph.D. degree in mechanical engineering from Nanyang Technology University, Singapore, in 2015.

Since 2018, he has worked with Shanghai Jiao Tong University, Shanghai, China, where he is currently appointed as an Associate Professor with the School of Mechanical Engineering. He has author or co-authored more than 50 publications. His research interests include soft robotics, 3-D and 4-D printing, and solid mechanics.

Chengru Jiang received the B.E. degree in process equipment and control engineering from the Dalian University of Technology, Dalian, China, in 2019. He is currently working toward the Ph.D. degree in mechanical engineering with School of Mechanical Engineering, Shanghai Jiao Tong University, Shanghai, China.

His research interests include theoretical modeling and design of soft robots, and integration of 3-D printed soft actuators and sensors.

Guoying Gu (Senior Member, IEEE) received the B.E. degree in electronic science and technology and the Ph.D. (Hons.) degree in mechatronic engineering from Shanghai Jiao Tong University, Shanghai, China, in 2006 and 2012, respectively.

He is currently appointed as a Distinguished Professor with the School of Mechanical Engineering, Shanghai Jiao Tong University. He was a Humboldt Fellow with University of Oldenburg, Oldenburg, Germany. He was a Visiting Scholar with the Massachusetts Institute of Technology, National University of Singapore, and Concordia University. He is the author or coauthor of more than 100 publications, which have appeared in *Science Robotics, Nature Biomedical Engineering, Nature Reviews Materials, Nature Materials, Nature Communications, Science Advances*, IEEE/ASME transactions, *Advanced Materials, Soft Robotics, Science China serials*, etc., as book chapters and in conference proceedings. His research interests include soft robotics, bioinspired and wearable robots, smart materials sensing, and actuation and motion control.

Dr. Gu was the recipient of the National Science Fund for Distinguished Young Scholars and the XPLORER PRIZE. He is an Associate Editor for Soft Robotics. He was an Associate Editor for IEEE TRANSACTIONS ON ROBOTICS AND IEEE ROBOTICS AND AUTOMATION LETTERS. He has also served for several journals as Editorial Board Member, Topic Editor, or Guest Editor, and several international conferences/symposiums as Chair, Co-Chair, Associate Editor, or Program Committee Member.